hippocampus-synthesized and circulation-derived sex steroids in the hippocampus. Endocrinology 2009; 150:5106–5112.
19. Nakanishi T, Nishikawa J, Hiromori Y, Yokoyama H, Koyanagi M, Takasuga S, Ishizaki J, Watanabe M, Isa S, Utoguchi N, Itoh N, Kohno Y, et al. Trialkyltin compounds bind retinoid X receptor to alter human placental endocrine functions. Mol Endocrinol 2005; 19:2502–2516.
20. Kanno J, Aisaki K, Igarashi K, Nakatsu N, Ono A, Kodama Y, Nagao T. "Per cell" normalization method for mRNA measurement by quantitative PCR and microarrays. BMC Genomics 2006; 7:64–77.
21. Ishii K, Imanaka-Yoshida K, Yoshida T, Sugimura Y. Role of stromal tenascin-C in mouse prostatic development and epithelial cell differentiation. Dev Biol 2008; 324:310–319.
22. Jakab RL, Horvath TL, Leranth C, Harada N, Naftolin F. Aromatase immunoreactivity in the rat brain: gonadectomy-sensitive hypothalamic neurons and an unresponsive "limbic ring" of the lateral septum-bed nucleus-amygdala complex. J Steroid Biochem Mol Biol 1993; 44:481–498.
23. Takeda Y, Liu X, Sumiyoshi M, Matsushima A, Shimohigashi M, Shimohigashi Y. Placenta expressing the greatest quantity of bisphenol A receptor ERRgamma among the human reproductive tissues: predominant expression of type-1 ERRgamma isoform. J Biochem 2009; 146:113–122.
24. vom Saal FS, Akingbemi BT, Belcher SM, Birnbaum LS, Crain DA, Eriksen M, Farabollini F, Guillette LJ Jr, Hauser R, Heindel JJ, Ho SM, Hunt PA, et al. Chapel Hill Bisphenol A Expert Panel Consensus Statement: integration of mechanisms, effects in animals and potential to impact human health at current levels of exposure. Reprod Toxicol 2007; 24:131–138.
25. Steinmetz R, Mitchner NA, Grant A, Allen DL, Bigsby RM, Ben-Jonathan N. The xenoestrogen bisphenol A induces growth, differentiation, and c-fos gene expression in the female reproductive tract. Endocrinology 1998; 139:2741–2747.
26. Milligan SR, Balasubramanian AV, Kalita JC. Relative potency of xenobiotic estrogens in an acute in vivo mammalian assay. Environ Health Perspect 1998; 106:23–26.
27. Colerangle JB, Roy D. Profound effects of the weak environmental estrogen-like chemical bisphenol A on the growth of the mammary gland of Noble rats. J Steroid Biochem Mol Biol 1997; 60:153–160.
28. Kawato S. Endocrine disrupters as disrupters of brain function: a neurosteroid viewpoint. Environ Sci 2004; 11:1–14.
29. Donjacour AA, Cunha GR. Stromal regulation of epithelial function. Cancer Treat Res 1991; 53:335–364.
30. Hayashi N, Cunha GR, Parker M. Permissive and instructive induction of adult rodent prostatic epithelium by heterotypic urogenital sinus mesenchyme. Epithelial Cell Biol 1993; 2:66–78.
31. Thomson AA. Role of androgens and fibroblast growth factors in prostatic development. Reproduction 2001; 121:187–195.
32. Timms BG, Lee CW, Aumuller G, Seitz J. Instructive induction of prostate growth and differentiation by a defined urogenital sinus mesenchyme. Microsc Res Tech 1995; 30:319–332.
33. Cunha GR. Age-dependent loss of sensitivity of female urogenital sinus to androgenic conditions as a function of the epithelia-stromal interaction in mice. Endocrinology 1975; 97:665–673.
34. Thomson AA, Timms BG, Barton L, Cunha GR, Grace OC. The role of smooth muscle in regulating prostatic induction. Development 2002; 129: 1905–1912.
35. Takayanagi S, Tokunaga T, Liu X, Okada H, Matsushima A, Shimohigashi Y. Endocrine disruptor bisphenol A strongly binds to human estrogen-related receptor gamma (ERRgamma) with high constitutive activity. Toxicol Lett 2006; 167:95–105.
36. Susens U, Hermans-Borgmeyer I, Borgmeyer U. Alternative splicing and expression of the mouse estrogen receptor-related receptor gamma. Biochem Biophys Res Commun 2000; 267:532–535.
37. Nakanishi T, Kohroki J, Suzuki S, Ishizaki J, Hiromori Y, Takasuga S, Itoh N, Watanabe Y, Utoguchi N, Tanaka K. Trialkyltin compounds enhance human CG secretion and aromatase activity in human placental choriocarcinoma cells. J Clin Endocrinol Metab 2002; 87:2830–2837.
38. Horiguchi T. Masculinization of female gastropod mollusks induced by organotin compounds, focusing on mechanism of actions of tributyltin and triphenyltin for development of imposex. Environ Sci 2006; 13:77–87.
39. Cunha GR, Donjacour A. Stromal-epithelial interactions in normal and abnormal prostatic development. Prog Clin Biol Res 1987; 239:251–272.
40. Richter CA, Taylor JA, Ruhlen RL, Welshons WV, Vom Saal FS. Estradiol and bisphenol A stimulate androgen receptor and estrogen receptor gene expression in fetal mouse prostate mesenchyme cells. Environ Health Perspect 2007; 115:902–908.
41. Ricke WA, McPherson SJ, Bianco JJ, Cunha GR, Wang Y, Risbridger GP. Prostatic hormonal carcinogenesis is mediated by in situ estrogen production and estrogen receptor alpha signaling. FASEB J 2008; 22: 1512–1520.

J Gastroenterol (2011) 46:339–349
DOI 10.1007/s00535-010-0355-9

ORIGINAL ARTICLE—ALIMENTARY TRACT

CITED2 is activated in ulcerative colitis and induces p53-dependent apoptosis in response to butyric acid

Tsutomu Yoshida · Tsukasa Sekine · Ken-ichi Aisaki · Tetuo Mikami · Jun Kanno · Isao Okayasu

Received: 13 June 2010 / Accepted: 21 November 2010 / Published online: 17 December 2010

Abstract
Background In ulcerative colitis (UC), *Fusobacterium varium* is significantly detected in patients' mucosa, and butyric acid (BA), abundantly produced by the bacterium, activates the p53 system and induces epithelial apoptosis, as we previously reported. However, factors active in the link between BA and p53 have yet to be clarified. Here, we identified a gene activated by BA specifically in UC-associated cancer cell lines and ascertained the mechanism of its activation of p53.
Methods cDNA microarray analysis based on the Percellome (per cell normalization) method was performed on BA-stimulated UC-associated cancers and sporadic colorectal cancer cell lines under conditions mimicking colonic epithelium UC. For validation of microarray results, molecular, biochemical, and histopathological analyses were performed.
Results We found the CBP/p300-interacting transactivator with glutamic acid/asparagine-rich carboxy-terminal domain 2 (CITED2) to be specifically upregulated in UC-associated cancer cell lines by BA treatment, at both mRNA and protein expression levels. CITED2 could be shown to induce p53 acetylation and p53-dependent apoptosis, accompanied by binding of CBP/p300. BA-dependent apoptosis was suppressed by an inhibitor of monocarboxylate transporter-1 and an siRNA for p53. In inflammatory foci of UC, histologically evident inflammatory activity and CITED2 expression were significantly correlated.
Conclusions CITED2 was identified as UC-associated protein by cDNA microarray based on the Percellome method under UC-mimicking conditions in vitro. CITED2 activation may induce mucosal apoptosis and erosion by activating p53 and thus play a critical role in linking enteric bacteria with mucosal inflammation in UC.

Keywords Ulcerative colitis · Inflammation · Apoptosis · CITED2 · Butyric acid · p53 · CBP/p300

The GeneChip data have been deposited in the Percellome project site (http://www.nihs.go.jp/tox/TtgPublication.htm) and are accessible with no restriction.

Electronic supplementary material The online version of this article (doi:10.1007/s00535-010-0355-9) contains supplementary material, which is available to authorized users.

T. Yoshida (✉) · T. Sekine · T. Mikami · I. Okayasu
Department of Pathology, Kitasato University School of Medicine, 1-15-1 Kitasato, Minami-ku, Sagamihara, Kanagawa 252-0374, Japan
e-mail: tyoshida@med.kitasato-u.ac.jp

K. Aisaki · J. Kanno
Division of Cellular and Molecular Toxicology, National Institute of Health Sciences, 1-18-1 Kamiyoga, Setagaya-ku, Tokyo 158-5801, Japan

Abbreviations

BA	Butyric acid
CITED2	CBP/p300-interacting transactivator with glutamic acid/asparagine-rich carboxy-terminal domain 2
4CHC	4-Hydroxycinnamate
IL-10	Interleukin-10
MCT1	Monocarboxylate transporter-1
q-RT-PCR	Quantitative reverse transcription PCR
sCRC	Sporadic colorectal cancer
UC	Ulcerative colitis
UCCA	Ulcerative colitis-associated cancer

Introduction

Ulcerative colitis (UC) is an intractable inflammatory bowel disease whose etiology is not known in detail. With long-standing UC, adenocarcinomas tend to occur in the colon, which might be due to repeated episodes of active chronic inflammation and remission [1, 2]. In a murine model system, dextran sulfate sodium (DSS) without mutagenicity induces UC-like colitis [3], and long-term repeated treatment with DSS can induce colitic cancers [4, 5]. Therefore, UC can be considered as a model disease for carcinogenesis on a background of chronic inflammation, and elucidation of the etiology of UC is important for treatment and prevention purposes.

The bacterial flora seem to constitute an important factor for triggering inflammation in UC, in accordance with previous reports concerning spontaneous development of UC-like colitis in IL-10 knockout mice under conventional breeding but not germ-free conditions [6–8]. Previously, we detected *Fusobacterium varium* (*F. varium*) by direct culture of mucosal biopsy specimens of UC patients and found intraepithelial invasion of *F. varium* to result in production of inflammatory cytokines in colonic epithelial cell lines in vitro [9, 10]. *F. varium* produces a short-chain fatty acid, butyric acid (BA), and direct luminal injection of BA into the rectum was found to induce apoptosis and UC-like lesions in mice [11]. In addition, BA activates p53-dependent apoptosis and DNA repair in vitro, and activation of p53 by its phosphorylation has been observed in situ in inflammatory foci of UC patients [12]. Clinically, we have shown significant improvement of UC by antibiotic combination therapy targeting *F. varium* [13, 14]. Recently, this was confirmed by a double-blind, placebo-controlled, multicenter trial [15]. However, the molecular mechanisms of BA-mediated p53 activation are unknown and largely remain to be elucidated.

In order to clarify this issue, we compared the genetic profiles of UC-associated carcinoma (UCCA) and sporadic colorectal adenocarcinoma (sCRC) cell lines undergoing BA treatment. Both series of cell lines were established in our laboratory [16]. The former include both p53 wild and mutant cells, whereas the latter are p53 wild. BA upregulates early response genes especially in UCCA cell lines, acting upstream of p53. Using whole genome cDNA microarray chips and the "per cell" normalization method (Percellome method) [17], we here identified genes specifically upregulated in UCCA lines with BA treatment. By detailed validation and the further examination, we focused on one upregulated gene, encoding the CBP/p300-interacting transactivator with glutamic acid/asparagine-rich carboxy-terminal domain 2 (CITED2) [18]. The protein itself activates p53 and its downstream molecules and accelerates apoptosis, and histological analysis revealed unique expression in the colonic mucosa of UC patients. Thus, we consider that CITED2 is an important and specific mediator of inflammation in UC, and might thus serve as a target of therapy.

Materials and methods

Cell lines and clinical cases

The human UCCA cell lines UCCA21, UCCA22, UCCA23, UCCA24, UCCA25 (p53 wild), and UCCA3 (p53 mutant), and the sCRC cell lines KE24, KE43w, and KE43p (p53 wild) were established in our laboratory [16], and cultured in Dulbecco's Modified Eagle Medium (GIBCO, Carlsbad, CA, USA) supplemented with 10% fetal bovine serum containing penicillin and streptomycin (GIBCO) at 37°C in 5% CO_2.

Microarray and data analysis

GeneChip analysis was conducted according to the Percellome method [17, 19] described in the Electronic Supplementary Material in detail. The GeneChip data have been deposited in the Percellome project site (http://www.nihs.go.jp/tox/TtgPublication.htm) and are accessible with no restriction. Differentially expressed genes were extracted by Fx algorithm [20], described in the Supplementary Methods online.

q-RT-PCR and western blotting

Total RNA was isolated from cells with an RNeasy kit (QIAGEN, Hilden, Germany), and 2-μg aliquots were used to synthesize cDNAs with a High Capacity cDNA Reverse Transcription Kit (Applied Biosystems, Foster City, CA, USA). Pre-amplified DNAs generated with a TaqMan PreAmp Master Mix Kit (Applied Biosystems) were used as templates for quantitative PCR with TaqMan Gene Expression Master Mix (Applied Biosystems) and FAM-dye-labelled TaqMan probe and primer sets for β-actin, CITED2, p53, CDKN1A (p21), Bax, MCT1, p53R2 (Applied Biosystems) using the 7500 real-time PCR system (Applied Biosystems). Quantitative PCR was performed as multiplex PCR with a VIC-dye-labelled β-actin probe and the fold ratio against VIC-labeled β-actin was calculated. All the quantitative RT-PCR (q-RT-PCR) studies were performed in triplex, and representative results for three independent experiments are shown.

Aliquots of 2×10^6 UCCA24 or KE43p cells after various treatments were lysed with lysis buffer (20 mM Tris–HCl, pH 7.6, 170 mM NaCl, 1 mM EDTA, 0.5% NP-40, 1 mM dithiothreitol). After separation by 12% SDS-

polyacrylamide gel electrophoresis and protein transfer to polyvinyl membranes, blocking with 5% bovine serum albumin was performed. Antibodies for CITED2 (Novous Biologicals, Inc Littleton, CO, USA), p53 (Novocastra Laboratories, Newcastle upon Tyne, UK), acetylated-p53 (Bio Academia, Osaka, Japan), $p21^{Cip1}$ (Santa Cruz Biotechnology, Santa Cruz, CA, USA), Bax (Transduction Laboratories, Lexington, KY, USA), and CBP/p300 (Santa Cruz) were used as first antibodies for western blotting. HRP-conjugated anti-mouse or HRP-conjugated anti-rabbit antibodies were then employed as secondary antibodies with ECL Western Blotting Detection Reagents (GE Healthcare, Buckinghamshire, UK) for visualization. Densitometry was performed by using ImageJ software (National Institutes of Health, USA)

Transfection and RNAi (siRNA) assays

Human CITED2 cDNA was obtained from Open Biosystems (Thermo Fisher Scientific, Huntsville, AL, USA, clone: LIFESEQ8724402) and subcloned into pcDNA-DEST40 (Invitrogen). Human CBP/p300 cDNA was also subcloned into the pcDNA-DEST40 vector. Transfection into UCCA24 and KE43p was achieved with Lipofectamin2000 (Invitrogen). siRNAs for CDKN1A, CITED2, HOXA1, SAT, TUBA3, and p53 (Ambion, Austin, TX, USA), and for non-sense control (Ambion) were transfected with the siPORT NeoFX Transfection Agent (Ambion).

Butyric acid treatment, detection of apoptosis, and MCT1 inhibition assays

Cultured cells were exposed to 2.5 mM BA as previously described [12]. Apoptosis was detected by the TUNEL method visualized by fluorescein isothiocyanate (FITC)-labeled digoxigenin according to the manufacturer's protocol with slight modifications using an ApopTag Plus Peroxidase In Situ Apoptosis Detection Kit (Intergen, Purchase, NY, USA). Apoptotic cells were counted and the percentages versus more than 100 DAPI (4′,6-diamino-2-phenylindole) positive cells were calculated. 0.5 mM 4-hydroxycinnamate (4CHC, Sigma, Saint Louis, MO, USA) was added to the culture medium for MCT1 inhibition assays.

Immunoprecipitation

Aliquots of 2×10^7 UCCA24 and KE43p cells were lysed in 1 ml of TNE buffer (10 mM Tris–HCl, pH 7.8, 1% nonidet-P 40, 0.15 M NaCl, 1 mM EDTA). After preprecipitation with protein G-Sepharose for 1 h at 4°C, lysates were incubated with 1 μg of anti-CITED2 antibody or anti-CBP/p300 for 1 h at 4°C followed by incubation with protein G-Sepharose for 1 h at 4°C. After centrifugation at 15,000 rpm for 5 min, the precipitants were washed with TNE buffer 5 times and denatured at 95°C. After SDS-polyacrylamide gel electrophoresis, they were subjected to western blotting with anti-CBP/p300 or anti-CITED2 antibodies.

Colorectal specimens and immunohistochemistry

A total of 102 surgically resected colorectal specimens from active and inactive UC patients and 20 from diverticulitis patients were obtained from the files of Kitasato University East Hospital and Kitasato University Hospital, and the histological activity of UC was determined according to the Matts' classification [21]: score 1, normal appearance; score 2, some infiltration of neutrophils in the mucosa; score 3, much cellular infiltration or presence of cryptitis; score 4, presence of crypt abscess and cellular infiltration; and score 5, presence of ulceration, erosion or necrosis, and cellular infiltration. Diverticulitis activity in diverticulosis was evaluated as none to mild and severe. Specimens were fixed with 10% formalin and embedded in paraffin. Semi-serial 4-μm-thick sections were cut for hematoxylin–eosin (H&E) staining and CITED2 immunohistochemistry with monoclonal anti-CITED2 antibodies (JA22, 1/1000, Novus Biologicals, Inc., Littleton, CO, USA) and an EnVision + kit (DakoCytomation, Glostrup, Denmark). After blocking endogenous peroxidase with 0.3% H_2O_2 in methanol, a 15-min microwave pretreatment in citrate buffer (pH 6.0, 0.01 mol/l) was performed for antigen retrieval, and after incubation with anti-CITED2 antibodies for 1 h at room temperature. 3,3′-Diaminobenzidine was applied as the final chromogen and faint nuclear counterstaining was finally achieved with methyl green. Scoring of immunoreactivity was performed as reported by Sinicrope et al. [22], and statistically analyzed by the Spearman's rank correlation test and Mann–Whitney's *U* test.

Results

Butyric acid upregulates the transcriptional expression of CITED2 specifically in UCCA lines

To identify genes upregulated by BA treatment specifically in UCCA lines, three UCCA and three sCRC lines were treated with 2.5 mM of BA (pH 7.4 in the culture medium). We earlier reported that the concentration of BA in the wells of Vero cell culture with *F. varium* was 6.42 mM (pH 6.90) [11], and 2.5 mM induced p53-mediated DNA repair [12]. The Percellome method enabled us to compare the mRNA expression profiles among the different cell lines per cell based on DNA content of each biosample. We applied the original algorithm (Fx) [20] and upregulated and

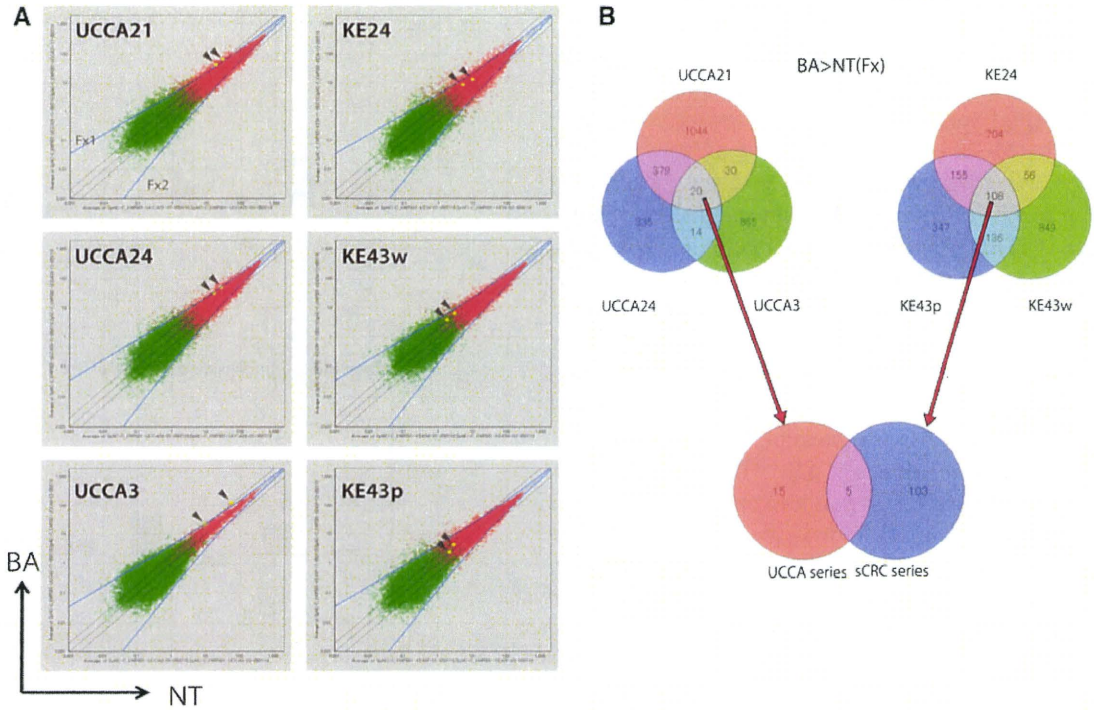

Fig. 1 **a** Genome-wide expression analysis after BA treatment. The analysis was performed by using the Affymetrix GeneChip Human Genome U133 plus 2.0 Array. Scatter plots are shown for BA treatment (BA) for 24 h and non-treatment (NT). The *open circles* show expression levels for each probe set. The *colors* indicate probabilities provided by the Affymetrix GeneChip Operation System: *red* means good and *green* means poor. The *yellow circles* show CITED2 probe sets for areas highlighted by *arrowheads*. The *black lines* show twofold, onefold, and 0.5-fold, respectively, and the *blue lines* indicate the empirical threshold levels (Fx1 and Fx2). The *spots above* the Fx1 and *below* the Fx2 line were evaluated as upregulated and downregulated, respectively ($p < 0.02$). **b** Venn diagrams of the upregulated probe sets in butyric acid (BA) treatment compared with non-treated (NT) controls in UCCA lines (UCCA21, UCCA24, and UCCA3) and sCRC lines (KE24, KE43p, and KE43w). *Numbers* of upregulated probe sets are indicated. Among the 20 and 108 probe sets upregulated in the UCCA and sCRC series, respectively, 5 were commonly upregulated in both. *Fx* Fx algorithm for the empirical threshold calculation

downregulated genes were listed at $p < 0.02$ (Fig. 1a). As compared with non-treated controls, 20 probe sets' genes were commonly upregulated in the UCCA lines, and 108 in the sCRC lines. Five were upregulated in both UCCA and sCRC lines, and 15 and 103 only in UCCA and sCRC lines, respectively (Fig. 1b). Of the 13 known genes contained in the 15 probe sets specifically upregulated only in UCCA lines, CITED2 was upregulated with 2 independent probe sets in the same GeneChip (see Table 1 for the gene list). As we previously found that the *F. varium*-BA system induces p53-dependent cellular responses [11, 12], we focused on whether p53-signaling might be influenced. As CITED2 was identified as a CBP/p300 binding protein which regulates p53 by acetylation [18, 23, 24], we considered that CITED2 might be a candidate and subjected it to further analyses.

CITED2 acts upstream of p53

q-RT-PCR showed increased upregulation of CITED2 in UCCA cell lines as compared with sCRC cell lines on BA

Table 1 Genes upregulated by BA treatment only in the UCCA series

Probe set ID	Gene symbol	GenBank ID
237156_at	–	–
204567_s_at	ABCG1	NM_004915
210431_at	ALPPL2	J04948
200982_s_at	ANXA6	NM_001155
207980_s_at	CITED2	NM_006079
209357_at	CITED2	NM_006079
202806_at	DBN1	NM_004395
215506_s_at	DIRAS3	AK021882
211538_s_at	HSPA2	U56725
203752_s_at	JUND	NM_005354
208581_x_at	MT1X	NM_005952
201599_at	OAT	NM_000274
201364_s_at	OAZ2	AF242521
35666_at	SEMA3F	U38276
204141_at	TUBB2	NM_001069

treatment, validating the microarray results (Fig. 2a). p53 downstream molecules, $p21^{Cip1}$ and Bax, were upregulated at the mRNA level, although p53 mRNA expression was not changed (Fig. 2b). The expression of monocarboxylate transporter-1 (MCT1), a transporter of BA, was also upregulated. When an siRNA for CITED2 was introduced into UCCA24 with or without BA treatment, it significantly suppressed CITED2 mRNA expression. Although p53 mRNA expression was upregulated by knockdown of CITED2 without BA treatment, this was abrogated by BA treatment with CITED2 knockdown, indicating an upstream location of CITED2 in the p53 signaling pathway (Fig. 2c). Suppression of CITED2 expression did not significantly affect the mRNA expression of p21, Bax, and p53R2, downstream molecules of p53, with or without BA treatment. CITED2 expression was also upregulated by BA treatment at the protein level in UCCA24 after 1–12 h, with a peak at 6 h, accompanied by p53 protein accumulation and followed by p21 and Bax expression (Fig. 3). Although Bax expression was high in the non-treatment state, Bcl-2 levels were also high and decreased with BA treatment. Upregulation of CITED2 was noted within 6 h of CITED2 transfection and p53 protein accumulation was observed in parallel. Thus, on treatment with BA, the p53 protein level was upregulated without transcriptional upregulation. As p53 downstream molecules were upregulated at the mRNA and protein levels, stabilization of p53 protein without transcriptional expression could account for this discrepancy. Therefore, CITED2 could be a candidate transducer of BA responsible for post-transcriptional upregulation of p53.

BA induces apoptosis through MCT1, CITED2, and p53

As we previously reported [12], BA induced apoptosis detected by the TUNEL method in the UCCA24 line (Fig. 4a, b). Apoptosis was abundantly induced by doxorubicin with wild-type p53 as previously reported [16]. It is well known that the doxorubicin-induced apoptosis is p53-dependent [25], and apoptosis was inhibited by an siRNA for p53, but not by non-sense siRNA. BA-induced apoptosis was inhibited by 4-hydroxycinnamate (4CHC), a specific inhibitor for MCT1 in both types of cell lines, and was also significantly inhibited by siRNA for p53. CITED2 overexpression also induced apoptosis in UCCA24, and this was partially and significantly reduced by p53 siRNA, but not by non-sense siRNA. As BA activates p53 by stabilization and does not induce transcriptional expression, the partial inhibition suggests reduction of the protein pool before BA treatment or CITED2 induction. The results indicate that BA induces apoptosis through MCT1, CITED2, and p53 activation. Although the BA-induced

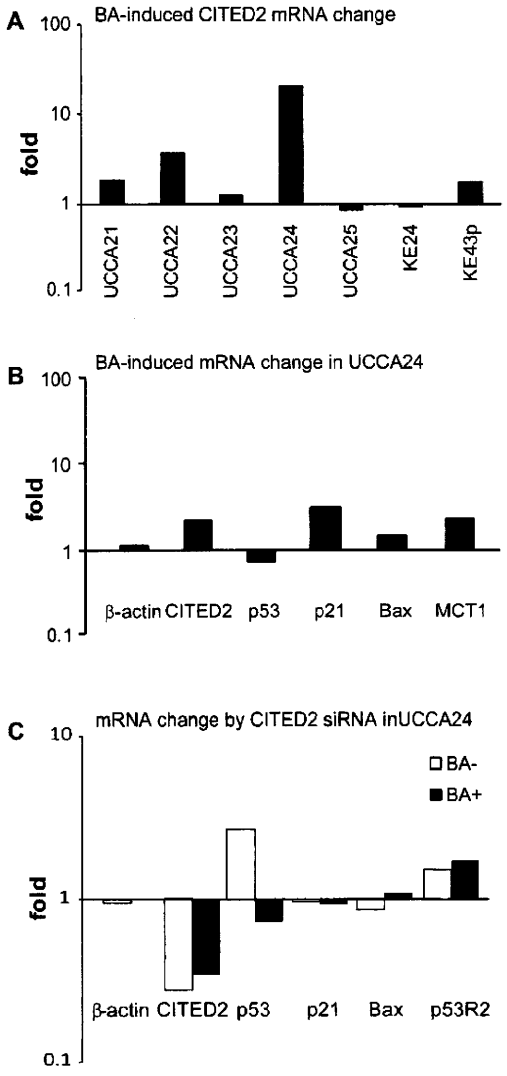

Fig. 2 q-RT-PCR for validation of CITED2 and p53-related genes, and knockdown effects of CITED2. Representative results for three independent experiments are shown. **a** CITED2 mRNA expression is induced by BA in UCCA cell lines. q-RT-PCR was performed after 2.5 mM BA was added for 24 h. UCCA cell lines, including UCCA 21 and 24 used for microarray analysis, tended to show upregulation of CITED2 mRNA expression against no BA treatment, whereas sCRC lines (KE24, KE43p) did not. **b** mRNA expression of p53-related molecules except p53 itself was increased in UCCA24 by BA treatment for 24 h, as analyzed by q-RT-PCR. Fold ratios of mRNA expression after 24 h BA treatment against no BA treatment are shown in the histogram. **c** siRNA for CITED2 was transfected 24 h before BA treatment in UCCA24. After BA treatment for 24 h, expression of β-actin, CITED2, p53, p21, Bax, and p53R2 was analyzed by q-RT-PCR. Fold expression of CITED2 siRNA transfected cells was compared with non-specific siRNA transfection. *Open* and *filled bars* show fold ratios for each gene against VIC-labeled β-actin expression with and without BA treatment

CITED2 level was almost equivalent to or greater than that in CITED2 transfected cells (Fig. 3a, b), the apoptosis level was much greater in CITED2 transfected cells (Fig. 4b).

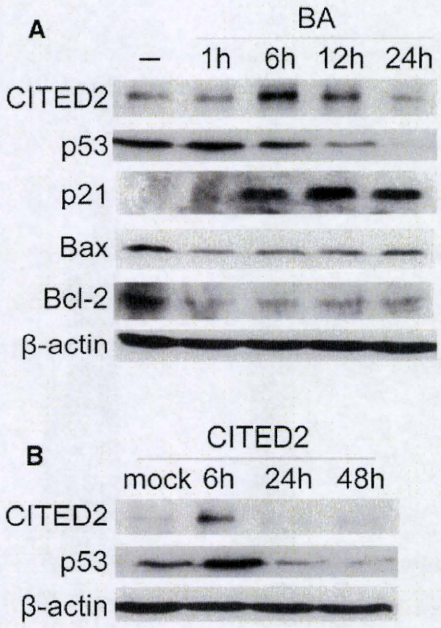

Fig. 3 CITED2, p53, and related protein expression with BA treatment and forced CITED2 expression in UCCA24. The indicated protein expression was analyzed by western blotting with BA treatment for 1, 6, 12, and 24 h (**a**) and CITED 2 transfection for 6, 24, and 48 h (**b**). CITED2 was transfected 24 h prior to BA treatment

This might be due to the direct effect of CITED2 by transfection whereas the apoptosis induced by BA could be regulated by other factors.

BA and CITED2 induce acetylation of p53 and increase protein expression

CITED2 has been identified as a co-factor for CBP/p300 [18], which induces apoptosis through acetylation of p53 [24, 26]. The amount of p53 protein was significantly increased along with the acetylated form of p53 with BA treatment (Fig. 5a) and CITED2 transfection (Fig. 5b). It is likely that CITED2 stabilizes p53 by its acetylation.

CITED2 binds to CBP/p300 in vitro

During BA treatment, we confirmed binding of CITED2 to CBP/p300 in vitro by immunoprecipitation (Fig. 5c). Binding was induced by CITED2 and CBP/p300 transfection as well as by BA treatment.

CITED2 is expressed in the surface epithelium of UC patients' colonic mucosa

Expression of CITED2 protein was evaluated in the colonic mucosa of UC patients in situ. The area (0–3) and the intensity (0–3) of CITED2 positivity were multiplied together and the correlation of the resulting CITED2 expression score with histological evidence of inflammation was assessed according to Matts (see Fig. 6a) [21]. CITED2 expression was localized in crypt bottoms of normal colonic mucosa. In contrast, it was found to be significantly increased in the surface lining epithelium and both upper and lower halves of the crypts in UC cases, whereas the increase of expression was limited to the lower halves in diverticulitis, with non-specific inflammation. In addition to the significant differences in expression score between histological grades by the Mann–Whitney's U test shown in Fig. 6b, a significant correlation of the increase of CITED2 expression with histological grade by Spearman's rank correlation test was also demonstrated, especially in lining epithelium and the upper halves of crypts ($\rho = 0.641$, $p < 0.0001$, lining epithelium, $\rho = 0.691$, $p < 0.0001$, upper crypts, $\rho = 0.460$, $p = 0.0002$, lower crypts).

Discussion

There have been many studies of the mechanisms underlying UC. Concerning roles of enterobacteria in UC development, bacterial invasion into the mucosal epithelia is considered to be associated with the production of cytokines, as a first step in inflammatory processes [10]. Thus, inflammatory cytokines produced by macrophages and lymphocytes in the stroma of the colonic mucosa are considered important factors. Interleukin-10 (IL-10)-deficient mice spontaneously develop UC-like colitis under conventional conditions, but not under specific pathogen- or germ-free conditions [6, 7]. To induce colitis in IL-10-deficient mice, commensal enteric bacteria are necessary [7]. Shkoda et al. [8] clearly revealed that IL-10 inhibits inflammation-induced endoplasmic reticulum (ER)-mediated stress responses by modulating activating transcription factor (ATF)-6 nuclear recruitment to the glucose-regulated ER stress protein-78 gene promoter in colonic epithelial cells. In inflammatory foci of UC, p53 is activated in the crypt epithelium [12], which suggests protective activity against inflammatory stress. Therefore, mutations of p53, frequently found in the early stages of UC-associated tumorigenesis, including non-tumorous regenerative mucosa, in contrast to the adenoma-carcinoma sequence [27], may greatly contribute to carcinogenesis. Short-chain fatty acids including BA are important to maintain colonic functions, and BA constitutes an energy supply for colonocytes and plays a central role in homeostasis of the colonic mucosa [28]. Previously, we detected *F. varium* by direct culture of UC patients' mucosa [14] and induced experimental UC in mice by intra-rectal administration of BA secreted from *F. varium* [9, 11]. In addition, BA induces DNA repair and apoptosis with the activation of

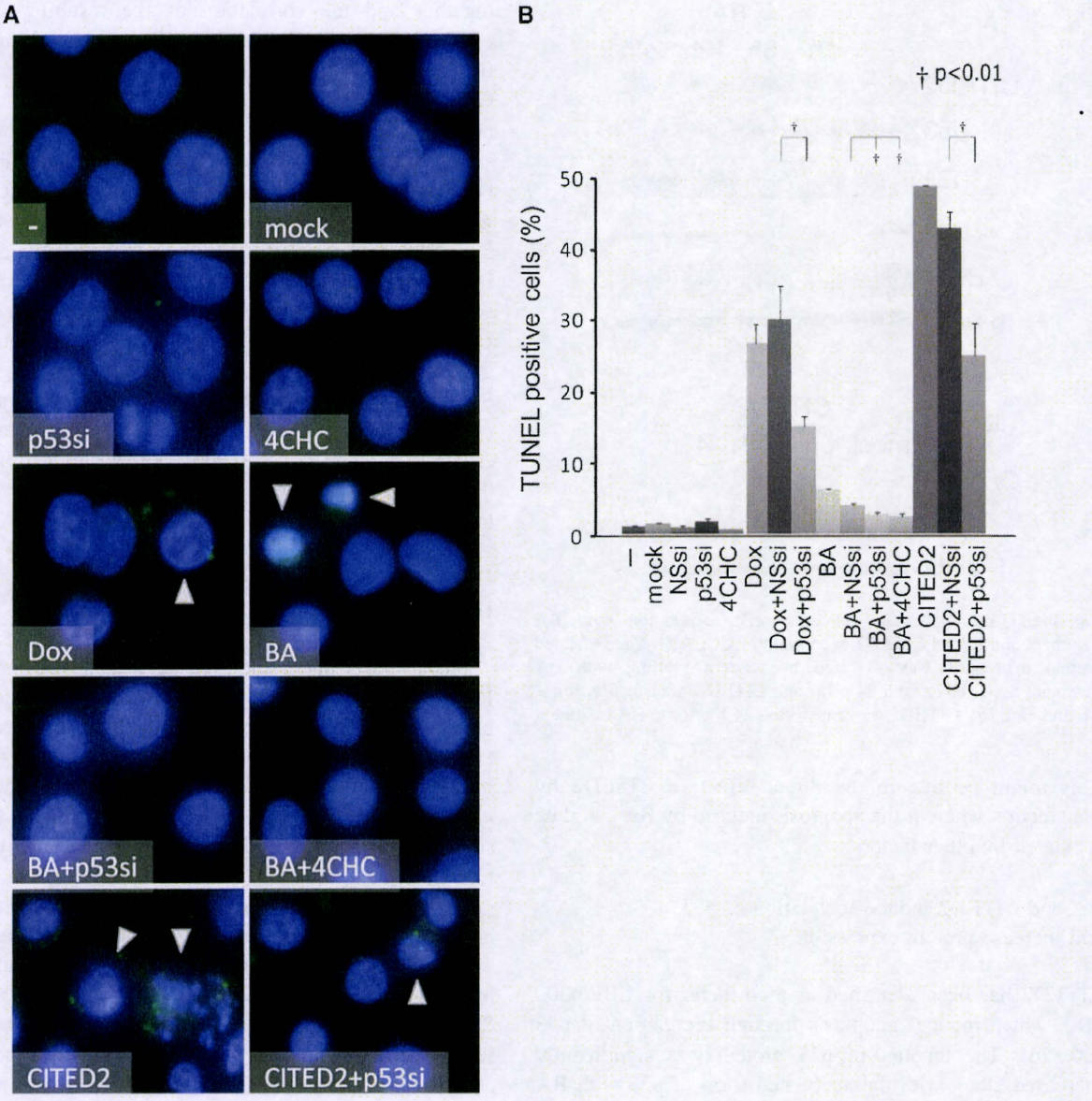

Fig. 4 Induction of p53-dependent apoptosis by BA treatment and CITED2 expression. **a** Representative images of apoptosis detected by the TUNEL method under various conditions in UCCA24 (*NT* no treatment, *Dox* treated with doxorubicin, *4CHC* treated with 4CHC, *BA* stimulated with BA, *BA + 4CHC* treated with both BA and 4CHC, *mock* mock transfection, *CITED2* CITED2 transfection). **b** Average percentages of apoptotic cells in three experiments in UCCA24 in the histogram with standard deviation bars. NSsi and p53si, siRNA for non-sense and p53 transfected, respectively. †Significant differences ($p < 0.01$) by Student's t test for each condition are also shown

p53–p53R2 system [12]. Therefore, BA would damage colonocytes in a high concentration condition. In order to mimic the inflammatory condition of UC in vitro, we used UCCA cell lines derived from human UC-associated adenocarcinomas [16]. Although UCCA lines are tumor cell lines and may have different characteristics from non-tumorous colonic epithelium, those used here are unique in being derived from a human UC background. As BA-induced apoptosis and activated p53-dependent DNA repair have been found in both sCRC and UCCA lines [11, 12], we here focused on their roles as a key factor for UC inflammation.

First, we established that mRNA expression of CITED2 and several other genes was upregulated by BA treatment in ulcerative colitis-associated cancer cell lines, but not in sporadic counterparts, by cDNA microarray analysis with the Percellome method [17]. Whereas two independent probe sets were listed as only upregulated in UCCA lines,

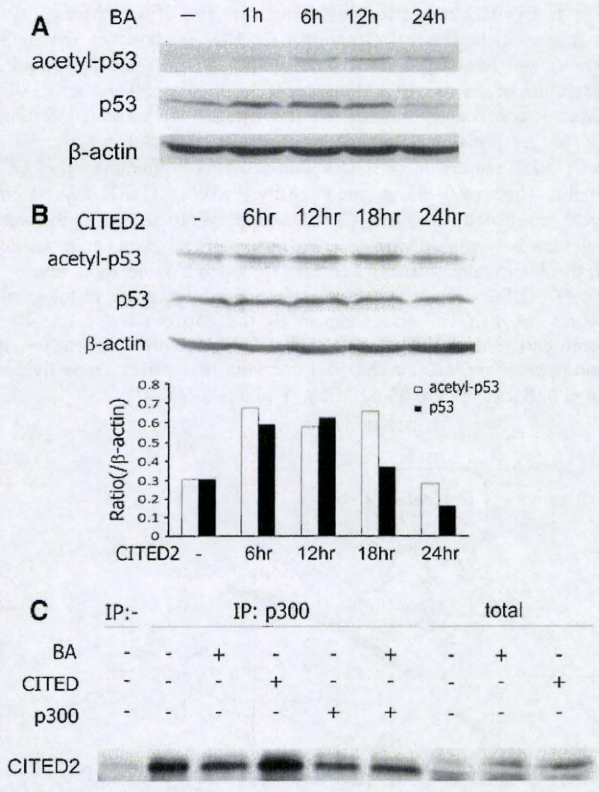

Fig. 5 Induction of p53 acetylation by BA and CITED2, accompanied by binding of CBP/p300 and CITED2 in UCCA24. **a** 2.5 mM BA treatment induced acetylation of p53 and increased the total amount of p53 from 1 to 24 h. **b** Transfection of CITED2 24 h prior to BA treatment for 24 h also induced acetylated p53 and increased the total amount of p53. A histogram of results for relative expression of acetylated p53 and p53 is shown *below*. Relative expression against *β*-actin was calculated by densitometry of western blot data. **c** Immunoprecipitation by anti-CBP/p300 antibody and immunoblotting with anti-CITED2 antibody showed binding of CITED2 and CBP/p300. *BA* indicates treatment by 2.5 mM BA for 24 h, *CITED2* and *p300* indicate the transfection of CITED2 and CBP/p300 24 h prior to the assay, respectively. A western blot from the total lysate is also illustrated

we especially focused on CITED2 among the 13 genes, because its function seemed to be closely related to p53 via CBP/p300 [18], with an upstream action. Indeed, RNAi analysis directly indicated that CITED2 is upregulated upstream of p53. Induction of CITED2 mRNA was not evident in several UCCA lines, such as UCCA23 and UCCA25 (Fig. 2). However, we confirmed the induction of CITED2 protein in those lines (data not shown) and the upregulation of CITED2 was statistically confirmed by the immunohistochemistry from the 102 inflammatory lesions of UC (Fig. 6).

Although CITED2 has been noted as an important factor for organ or tissue development [29, 30], it was originally found to inhibit the binding to hypoxia-inducible factor 1 (HIF1) [31]. Bakker et al. [32] reported CITED2 to be transcriptionally induced by FOXO3a, a member of the FOXO subfamily of Forkhead transcription factors, and to inhibit HIF1-induced apoptosis in hypoxia, which is proposed as a survival response of cancer cells. Although HIF1 induces p53-dependent apoptosis [33–35], it also causes p53-independent apoptosis via BNIP3 and NIX induction [34–36]. As Bakker et al. used p53 wild-type cell lines, it was uncertain whether CITED2 inhibited p53-dependent HIF1-induced apoptosis. In the present study, however, BA and CITED2 clearly induced apoptosis, which was inhibited by an siRNA for p53. Furthermore, the BA-induced apoptosis was inhibited by an inhibitor of MCT1, through which BA is transported into the cytoplasm [37, 38], and an siRNA for p53 partially but significantly inhibited the BA- and CITED2-induced apoptosis. Apoptosis induced by CITED2 transfection was more frequent than by BA treatment (Fig. 4b), although the BA-induced CITED2 level was almost equivalent to or greater than that in CITED2 transfected cells (Fig. 3a, b). This might be due to a direct effect of CITED2 by transfection or to apoptosis induced by BA being regulated by other factors. The dependence of BA-induced apoptosis on MCT1, demonstrated by 4CHC, an inhibitor of MCT1, should be verified by other approaches. Although protein stabilization of p53 was apparent on BA treatment with CITED2 overexpression, knockdown of p53 at the mRNA level could also inhibit the BA–CITED2 pathway. Therefore, CITED2 possibly plays different roles in BA-induced and HIF1-induced apoptosis, which might depend on modulation of the phosphorylation or acetylation sites of p53.

According to recent studies, p53 induces apoptosis via acetylation of lysine 120 on DNA damage or in response to stress signaling with CBP/p300 binding [24, 26]. The acetylated form of p53 is stable with regard to the Mdm2-ubiquitination system [39]. We here demonstrated acetylation of p53 by BA treatment and forced CITED2 expression accompanied by p53 protein accumulation (Fig. 5a, b). At the same time, binding of the CITED2 and CBP/p300 was also observed by immunoprecipitation (Fig. 5c). Therefore, we conclude that CITED2 is upregulated by BA, in turn activating p53-dependent apoptosis via acetylation of p53 protein (Fig. 7). Although transcription of p53 was not observed, the data support p53 protein stabilization by BA and CITED2. Further investigation of the half-life of p53 after BA treatment with or without CITED2 knockdown should clarify this point.

In UC, p53 gene alteration is observed even in non-tumorous regenerative epithelium [27]. In addition, p53 expression is upregulated in inflammatory foci of UC without gene mutation and the p53 and p53R2 DNA repair system is accelerated [12]. Therefore, the repair capacity may be overloaded in active UC. We previously found greater upregulation of Bax protein in UCCA as compared

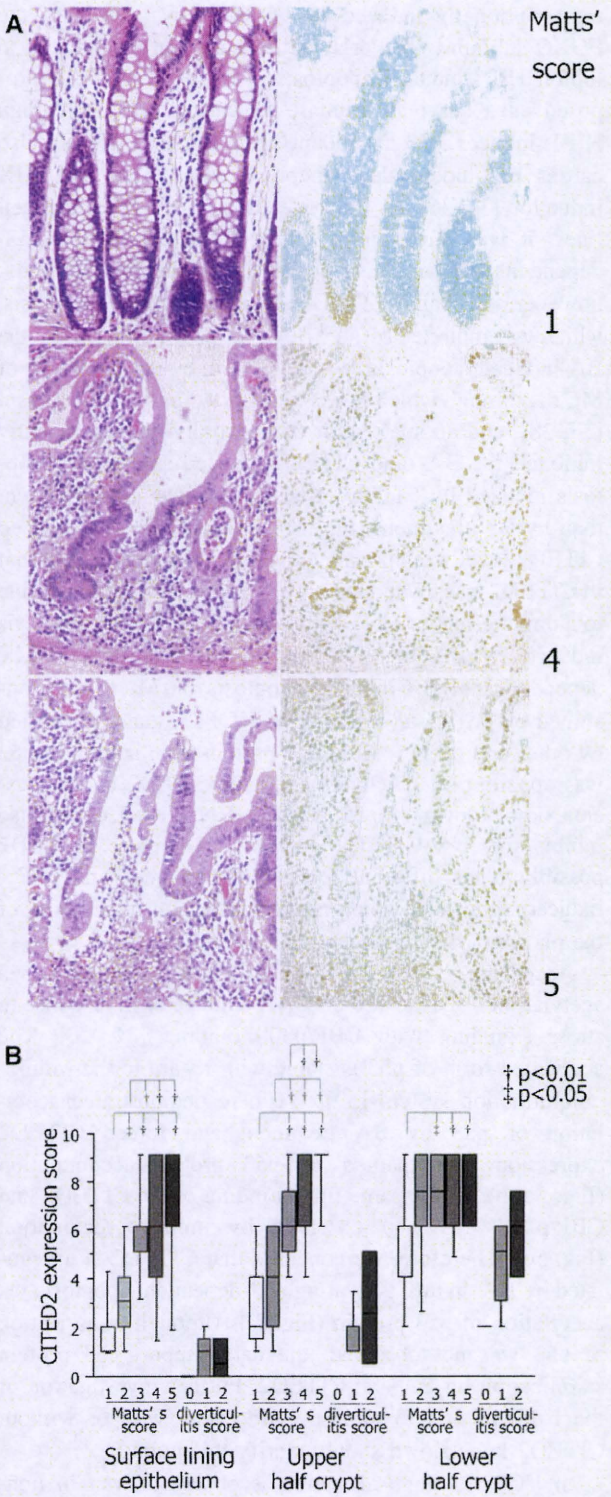

Fig. 6 CITED2 expression in inflammatory foci of ulcerative colitis. **a** Immunohistochemical staining of CITED2 is shown in the *right panels* and semi-serial H&E sections are shown in the *left panels*. Examples of inactive UC (Matts' score 1, *upper panel*) and active UC (Matts' score 4 and 5, *middle* and *lower panel*) are presented. Strong CITED2 expression is remarkable in epithelial nuclei in active UC. **b** CITED2 expression correlates with activity of inflammation of UC in situ. The area (0–3) and the intensity (0–3) of CITED2 expression were evaluated and the CITED2 expression score (0–9) was calculated by multiplying the two results. The inflammatory grade of the diverticulosis cases was scored from 0 to 2 (none, mild, severe). The CITED2 expression scores are shown along with histological scores. Median values are shown by the *horizontal line*, the *box* represents values between the 25th and 75th percentiles, and the *lower* and *upper bars* indicate the 10th and 90th percentiles, respectively. $^{\dagger}p < 0.01$ and $^{\ddagger}p < 0.05$ by Mann–Whitney's *U* test

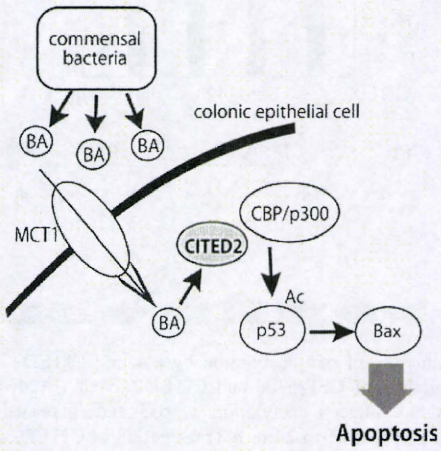

Fig. 7 Scheme for BA-induced apoptosis. BA produced by commensal bacteria, such as *F. varium*, is incorporated by MCT1 and induces CITED2 expression. The CITED2-CBP/p300 complex then acetylates p53 which stabilizes the protein, resulting in upregulated transcription of proapoptotic genes including Bax, and induction of apoptosis. Apoptosis of colonic epithelial cells leads to erosion of the mucosa, so that bacteria can more easily colonize. *Ac* acetylation; *BA* butyric acid; *MCT1* monocarboxylate transporter-1

with sCRC [40], which might have a similar effect. Matts' histological scores based on the infiltration of neutrophils and the presence of cryptitis, crypt abscess and erosion, reflect the inflammation activity of UC [21]. The fact that CITED2 expression in UC is also increased in the upper halves of the crypts and positively correlated with the histological activity of UC, evaluated by Matts' histological scores, is clear evidence of an association with UC inflammation. In contrast, although the CITED2 expression was increased in the inflammatory foci of diverticulitis, the expression score was almost at the same level as that of the inactive UC (Matts' score 1). This might indicate that the BA-CITED2 system is specifically involved in the UC inflammation, and not under conditions of non-specific colonic inflammation such as diverticulitis.

Previously, we showed that specific enterobacteria including *F. varium* are frequently detectable in UC patients' mucosa. Here we showed BA-induced apoptosis via CITED2 induction and p53 activation, and that CITED2 expression clearly correlates with histological UC

activity. Although the reported role of CITED2 in hypoxic stress does not coincide with our present results [32], our present histopathological study supports a scenario in human UC involving another CITED2-activating pathway. Thus, highly concentrated BA produced by enteric bacteria would induce CITED2-p53-dependent apoptosis in the colonic epithelium and cause erosion, which is typical of active UC. With mucosal erosion, enteric bacteria can easily infiltrate into the colonic stroma and stimulate macrophages [41], which would enhance inflammation by producing inflammatory cytokines. Apoptosis induced by BA was here inhibited by an siRNA for p53, as well as by 4CHC, an inhibitor of MCT1 (Fig. 4b), which suggests the possibility of anti-inflammation targeted therapy. However, mechanisms of UC generation still need further analysis, particular with regard to enteric bacteria. In conclusion, we propose that p53 activation via CITED2 upregulation by BA and consequent p53 acetylation is a possible mechanism underlying UC development.

Acknowledgments The authors appreciate the technical assistance of Ms. Y. Numata and would like to thank Dr. M. Moore for revising the English of the manuscript. This work was supported in part by Grants-in-Aid for Scientific Research from the Japan Society for the Promotion of Science, Health Sciences Research Grants H18-Kagaku-Ippan-001 from the Ministry of Health, Labour and Welfare, Japan, Grants-in-Aid from Kitasato University Graduate School of Medical Sciences and Kanagawa Nanbyo Foundation.

Conflicts of interest The authors disclose no conflicts with this work.

References

1. Arai N, Mitomi H, Ohtani Y, Igarashi M, Kakita A, Okayasu I. Enhanced epithelial cell turnover associated with p53 accumulation and high p21WAF1/CIP1 expression in ulcerative colitis. Mod Pathol. 1999;12:604–11.
2. Mitsuhashi J, Mikami T, Saigenji K, Okayasu I. Significant correlation of morphological remodeling in ulcerative colitis with disease duration and between elevated p53 and p21 expression in rectal mucosa and neoplastic development. Pathol Int. 2005;55: 113–21.
3. Okayasu I, Hatakeyama S, Yamada M, Ohkusa T, Inagaki Y, Nakaya R. A novel method in the induction of reliable experimental acute and chronic ulcerative colitis in mice. Gastroenterology. 1990;98:694–702.
4. Okayasu I, Ohkusa T, Kajiura K, Kanno J, Sakamoto S. Promotion of colorectal neoplasia in experimental murine ulcerative colitis. Gut. 1996;39:87–92.
5. Okayasu I, Yamada M, Mikami T, Yoshida T, Kanno J, Ohkusa T. Dysplasia and carcinoma development in a repeated dextran sulfate sodium-induced colitis model. J Gastroenterol Hepatol. 2002;17:1078–83.
6. Kuhn R, Lohler J, Rennick D, Rajewsky K, Muller W. Interleukin-10-deficient mice develop chronic enterocolitis. Cell. 1993;75: 263–74.
7. Sellon RK, Tonkonogy S, Schultz M, Dieleman LA, Grenther W, Balish E, et al. Resident enteric bacteria are necessary for development of spontaneous colitis and immune system activation in interleukin-10-deficient mice. Infect Immun. 1998;66:5224–31.
8. Shkoda A, Ruiz PA, Daniel H, Kim SC, Rogler G, Sartor RB, et al. Interleukin-10 blocked endoplasmic reticulum stress in intestinal epithelial cells: impact on chronic inflammation. Gastroenterology. 2007;132:190–207.
9. Ohkusa T, Sato N, Ogihara T, Morita K, Ogawa M, Okayasu I. *Fusobacterium varium* localized in the colonic mucosa of patients with ulcerative colitis stimulates species-specific antibody. J Gastroenterol Hepatol. 2002;17:849–53.
10. Ohkusa T, Yoshida T, Sato N, Watanabe S, Tajiri H, Okayasu I. Commensal bacteria can enter colonic epithelial cells and induce proinflammatory cytokine secretion: a possible pathogenic mechanism of ulcerative colitis. J Med Microbiol. 2009;58:535–45.
11. Ohkusa T, Okayasu I, Ogihara T, Morita K, Ogawa M, Sato N. Induction of experimental ulcerative colitis by *Fusobacterium varium* isolated from colonic mucosa of patients with ulcerative colitis. Gut. 2003;52:79–83.
12. Yoshida T, Haga S, Numata Y, Yamashita K, Mikami T, Ogawa T, et al. Disruption of the p53–p53r2 DNA repair system in ulcerative colitis contributes to colon tumorigenesis. Int J Cancer. 2006;118:1395–403.
13. Ohkusa T, Nomura T, Terai T, Miwa H, Kobayashi O, Hojo M, et al. Effectiveness of antibiotic combination therapy in patients with active ulcerative colitis: a randomized, controlled pilot trial with long-term follow-up. Scand J Gastroenterol. 2005;40: 1334–42.
14. Nomura T, Ohkusa T, Okayasu I, Yoshida T, Sakamoto M, Hayashi H, et al. Mucosa-associated bacteria in ulcerative colitis before and after antibiotic combination therapy. Aliment Pharmacol Ther. 2005;21:1017–27.
15. Ohkusa T, Kato K, Terao S, Chiba T, Mabe K, Murakami K, et al. Newly developed antibiotic combination therapy for ulcerative colitis: a double-blind placebo-controlled multicenter trial. Am J Gastroenterol. 2010;105:1820–9.
16. Yamashita K, Yasuda S, Kuba T, Otani Y, Fujiwara M, Okayasu I. Unique characteristics of rectal carcinoma cell lines derived from invasive carcinomas in ulcerative colitis patients. Cancer Sci. 2004;95:211–7.
17. Kanno J, Aisaki K, Igarashi K, Nakatsu N, Ono A, Kodama Y, et al. "Per cell" normalization method for mRNA measurement by quantitative PCR and microarrays. BMC Genomics. 2006;7:64.
18. Leung MK, Jones T, Michels CL, Livingston DM, Bhattacharya S. Molecular cloning and chromosomal localization of the human CITED2 gene encoding p35srj/Mrg1. Genomics. 1999;61: 307–13.
19. Sanosaka T, Namihira M, Asano H, Kohyama J, Aisaki K, Igarashi K, et al. Identification of genes that restrict astrocyte differentiation of midgestational neural precursor cells. Neuroscience. 2008;155:780–8.
20. Aisaki K, Aizawa S, Fujii H, Kanno J, Kanno H. Glycolytic inhibition by mutation of pyruvate kinase gene increases oxidative stress and causes apoptosis of a pyruvate kinase deficient cell line. Exp Hematol. 2007;35:1190–200.
21. Matts SG. The value of rectal biopsy in the diagnosis of ulcerative colitis. Q J Med. 1961;30:393–407.
22. Sinicrope FA, Lemoine M, Xi L, Lynch PM, Cleary KR, Shen Y, et al. Reduced expression of cyclooxygenase 2 proteins in hereditary nonpolyposis colorectal cancers relative to sporadic cancers. Gastroenterology. 1999;117:350–8.
23. Braganca J, Eloranta JJ, Bamforth SD, Ibbitt JC, Hurst HC, Bhattacharya S. Physical and functional interactions among AP-2 transcription factors, p300/CREB-binding protein, and CITED2. J Biol Chem. 2003;278:16021–9.

24. Kruse JP, Gu W. Modes of p53 regulation. Cell. 2009;137: 609–22.
25. Lowe SW, Ruley HE, Jacks T, Housman DE. p53-dependent apoptosis modulates the cytotoxicity of anticancer agents. Cell. 1993;74:957–67.
26. Vousden KH, Prives C. Blinded by the light: the growing complexity of p53. Cell. 2009;137:413–31.
27. Yoshida T, Mikami T, Mitomi H, Okayasu I. Diverse p53 alterations in ulcerative colitis-associated low-grade dysplasia: full-length gene sequencing in microdissected single crypts. J Pathol. 2003;199:166–75.
28. Scheppach W. Effects of short chain fatty acids on gut morphology and function. Gut. 1994;35:S35–8.
29. Sperling S, Grimm CH, Dunkel I, Mebus S, Sperling HP, Ebner A, et al. Identification and functional analysis of CITED2 mutations in patients with congenital heart defects. Hum Mutat. 2005;26:575–82.
30. Qu X, Lam E, Doughman YQ, Chen Y, Chou YT, Lam M, et al. Cited2, a coactivator of HNF4alpha, is essential for liver development. EMBO J. 2007;26:4445–56.
31. Bhattacharya S, Michels CL, Leung MK, Arany ZP, Kung AL, Livingston DM. Functional role of p35srj, a novel p300/CBP binding protein, during transactivation by HIF-1. Genes Dev. 1999;13:64–75.
32. Bakker WJ, Harris IS, Mak TW. FOXO3a is activated in response to hypoxic stress and inhibits HIF1-induced apoptosis via regulation of CITED2. Mol Cell. 2007;28:941–53.
33. Suzuki H, Tomida A, Tsuruo T. Dephosphorylated hypoxia-inducible factor 1alpha as a mediator of p53-dependent apoptosis during hypoxia. Oncogene. 2001;20:5779–88.
34. Harris AL. Hypoxia—a key regulatory factor in tumour growth. Nat Rev Cancer. 2002;2:38–47.
35. Greijer AE, van der Wall E. The role of hypoxia inducible factor 1 (HIF-1) in hypoxia induced apoptosis. J Clin Pathol. 2004;57: 1009–14.
36. Sowter HM, Ratcliffe PJ, Watson P, Greenberg AH, Harris AL. HIF-1-dependent regulation of hypoxic induction of the cell death factors BNIP3 and NIX in human tumors. Cancer Res. 2001; 61:6669–73.
37. Garcia CK, Li X, Luna J, Francke U. cDNA cloning of the human monocarboxylate transporter 1 and chromosomal localization of the SLC16A1 locus to 1p13.2–p12. Genomics. 1994;23:500–3.
38. Cuff M, Dyer J, Jones M, Shirazi-Beechey S. The human colonic monocarboxylate transporter Isoform 1: its potential importance to colonic tissue homeostasis. Gastroenterology. 2005;128:676–86.
39. Gu W, Roeder RG. Activation of p53 sequence-specific DNA binding by acetylation of the p53 C-terminal domain. Cell. 1997;90:595–606.
40. Yoshida T, Matsumoto N, Mikami T, Okayasu I. Upregulation of p16(INK4A) and Bax in p53 wild/p53-overexpressing crypts in ulcerative colitis-associated tumours. Br J Cancer. 2004;91: 1081–8.
41. Ohkusa T, Okayasu I, Tokoi S, Ozaki Y. Bacterial invasion into the colonic mucosa in ulcerative colitis. J Gastroenterol Hepatol. 1993;8:116–8.

Development 137, 1515-1522 (2010) doi:10.1242/dev.044545

The oscillation of Notch activation, but not its boundary, is required for somite border formation and rostral-caudal patterning within a somite

Masayuki Oginuma[1,2,*], Yu Takahashi[3,*], Satoshi Kitajima[3], Makoto Kiso[2], Jun Kanno[3], Akatsuki Kimura[1,4] and Yumiko Saga[1,2,†]

SUMMARY

Notch signaling exerts multiple roles during different steps of mouse somitogenesis. We have previously shown that segmental boundaries are formed at the interface of the Notch activity boundary, suggesting the importance of the Notch on/off state for boundary formation. However, a recent study has shown that mouse embryos expressing Notch-intracellular domain (NICD) throughout the presomitic mesoderm (PSM) can still form more than ten somites, indicating that the NICD on/off state is dispensable for boundary formation. To clarify this discrepancy in our current study, we created a transgenic mouse lacking NICD boundaries in the anterior PSM but retaining Notch signal oscillation in the posterior PSM by manipulating the expression pattern of a Notch modulator, lunatic fringe. In this mouse, clearly segmented somites are continuously generated, indicating that the NICD on/off state is unnecessary for somite boundary formation. Surprisingly, this mouse also showed a normal rostral-caudal compartment within a somite, conferred by a normal Mesp2 expression pattern with a rostral-caudal gradient. To explore the establishment of normal Mesp2 expression, we performed computer simulations, which revealed that oscillating Notch signaling induces not only the periodic activation of *Mesp2* but also a rostral-caudal gradient of Mesp2 in the absence of striped Notch activity in the anterior PSM. In conclusion, we propose a novel function of Notch signaling, in which a progressive oscillating wave of Notch activity is translated into the rostral-caudal polarity of a somite by regulating *Mesp2* expression in the anterior PSM. This indicates that the initial somite pattern can be defined as a direct output of the segmentation clock.

KEY WORDS: Notch signaling, Hes7, Mesp2, Segmentation clock, Presomitic mesoderm, Lunatic fringe, Somitogenesis

INTRODUCTION

The periodicity of the segmented somites is established in the posterior presomitic mesoderm (PSM) via the function of a so-called molecular clock, which is based on complex gene regulatory networks under the control of three major signaling pathways: Notch, Fgf and Wnt (Dequeant et al., 2006; Dequeant and Pourquie, 2008). Among these pathways, Fgf and Wnt are implicated in the maintenance of immature PSM cells (Aulehla et al., 2003; Aulehla et al., 2008; Wahl et al., 2007; Delfini et al., 2005; Niwa et al., 2007), whereas Notch signaling might be directly involved in the generation of periodicity (Oginuma et al., 2008; Yasuhiko et al., 2006; Takahashi et al., 2000; Takahashi et al., 2003). In mice, Notch signal oscillations are produced by the suppressive function of the glycosyltransferase lunatic fringe (Lfng) as the levels of activated Notch1 (cleaved form of the Notch1 intracellular domain, referred to as cNICD hereafter) are upregulated in the *Lfng*-null mouse embryo (Morimoto et al., 2005). The expression of *Lfng* exhibits a biphasic pattern involving oscillation in the posterior PSM and a stabilized striped pattern in the anterior PSM (Aulehla and Johnson, 1999; McGrew et al., 1998; Morales et al., 2002; Cole et al., 2002). The oscillatory expression of *Lfng* is positively regulated by Notch signaling as it is greatly downregulated in *Dll1*-null mice, whereas it is negatively regulated by Hes7 as revealed by its upregulation in *Hes7*-null embryos (Barrantes et al., 1999; Bessho et al., 2003; Morales et al., 2002). The stabilized expression of *Lfng* is under the control of the Mesp2 transcription factor and stabilization does not occur in the absence of Mesp2 (Morimoto et al., 2005). In the absence of Lfng, no clear segmental border is defined and the rostral-caudal (R-C) compartmentalization within a somite is randomized (Zhang and Gridley, 1998; Evrard et al., 1998).

In the anterior PSM, the Mesp2 transcription factor plays an important role in the creation of a cNICD on/off state that corresponds to the future segmental boundary via the activation of Lfng transcription (Morimoto et al., 2005). This suggests that the Notch on/off state is important for boundary formation. However, a recent study has shown that mouse embryos expressing Notch activity throughout the PSM still show the ability to form more than ten somites, indicating that the Notch on/off state is dispensable for boundary formation (Feller et al., 2008). By contrast, however, other studies have reported that transgenic mice expressing *Lfng* only in the anterior PSM show normal segmental border formation after embryonic day 10.5 (E10.5), suggesting that the Notch on-off state generated in the anterior PSM is sufficient to create a somite boundary at least in the later stage embryos (Shifley et al., 2008; Stauber et al., 2009).

To resolve this discrepancy, we have, in our current study, generated a mouse that lacks the anterior striped Lfng expression pattern, but at the same time retains oscillating Lfng activity in the

[1]Department of Genetics, SOKENDAI, 1111 Yata, Mishima, Shizuoka 411-8540, Japan. [2]Division of Mammalian Development, National Institute of Genetics, Yata 1111, Mishima 411-8540, Japan. [3]Division of Cellular and Molecular Toxicology, National Institute of Health Sciences, 1-18-1 Kamiyoga, Setagaya-ku, Tokyo 158-8501, Japan. [4]Cell Architecture Laboratory, National Institute of Genetics, Yata 1111, Mishima 411-8540, Japan.

*These authors contributed equally to this work
†Author for correspondence (ysaga@lab.nig.ac.jp)

Accepted 17 February 2010

posterior PSM. The resulting transgenic mouse shows no clear cNICD on/off state in the anterior PSM. Nevertheless, this mouse exhibits normal boundary formation, indicating that the cNICD boundary is dispensable for somite formation. In addition, our transgenic mouse shows normal R-C patterning within a somite. Further analyses by computer simulation have led us to conclude that Notch signaling oscillation functions as an output signal that is both required and sufficient to establish the *Mesp2* expression pattern needed for normal somitogenesis.

MATERIALS AND METHODS

Animals

The wild-type mice used in this study were the MCH strain (a closed colony established at CLEA, Japan). The *Lfng*-null (Evrard et al., 1998), *Mesp2*-null (*Mesp2*$^{MCM/+}$) (Takahashi et al., 2007) and *Mesp2-lacZ* (*Mesp2*$^{lacZ/+}$) (Takahashi et al., 2000) mouse lines are maintained in the animal facility of the National Institute of Genetics and National Institute of Health Sciences, Japan.

Gene targeting strategy to generate the *Mesp2*^{Lfng} allele

The knock-in strategy used to target the *Mesp2* locus is largely similar to our previously described method (Takahashi et al., 2000), except that *Lfng* cDNA was inserted. The *pgk-neo* cassette flanked by a *lox* sequence was removed by crossing with *CAG-Cre* mice (Sakai and Miyazaki, 1997).

Generation of the *Hes7-Lfng* transgenic mice

We used a 12 kb *Hes7* gene cassette comprising 5 kb of upstream sequence and all of the exons and introns, as this construct had previously been confirmed to be sufficient to reproduce the endogenous *Hes7* oscillation pattern when inserted in-frame at the translational start site (Kageyama et al., personal communications). We generated the construct *Lfng IRES-EGFP*, in which *IRES* (internal ribosomal entry site)-*EGFP* (enhanced GFP) was fused to the 3′ end of *Lfng* cDNA, and inserted this construct into the *Hes7*-translational initiation site. The resulting DNA was digested with restriction enzymes to remove vector sequences and gel purified. Transgenic mice were generated by microinjection of this construct into fertilized eggs, which were then transferred into the oviducts of pseudopregnant foster females.

In situ hybridization, immunohistochemistry, histology and skeletal preparations

The methods used for wholemount in situ hybridization, section in situ hybridization, immunohistochemistry, histology and skeletal preparation by Alcian Blue/Alizarin Red staining are described in our previous reports (Morimoto et al., 2005; Oginuma et al., 2008; Takahashi et al., 2000). The cNICD signal was detected by immunohistochemistry using anti-cleaved NICD (Val1744; 1:500; Cell Signaling Technology). Probes were prepared also as described previously: *Mesp2* exon-intron (Oginuma et al., 2008), *Mesp2* (Takahashi et al., 2000) and *Lfng* (Evrard et al., 1998). The *GFP* cRNA probe was prepared by PCR-amplification of *GFP* cDNA.

Computer simulation

Our computer simulation model is based on the previous mathematical description of a clock-and-wavefront model constructed by J. Lewis (Palmeirim et al., 1997). By using the basic oscillating function in the Lewis model, we modeled the activity of cNICD, n, at given time, t, and anteroposterior position, x, as:

$$n(x,t)=\left[1-\cos\left\{2\pi\int_0^t\frac{1}{1+e^{(x+t)/2}}dt\right\}\right]/2\,.$$

For the control simulation with constant activity of cNICD, the cNICD activity, n, was set to 0.3. For the simulation with oscillating cNICD without wave, n was formulated as $n(x,t)=\{1-\cos(\pi t)\}/2$. The activity of Fgf8 is known to gradually decrease from posterior to anterior, and also according to the time elapsed. These features of Fgf8 fit well with the formulation of the clock cycling rate in the Lewis model and, thus, we calculated the activity of Fgf8, f, using the formula $f(x,t)=1/(1+e^{(x+t)/2})$.

We next added the regulation of Mesp2 and Tbx6 expression to the model. As cNICD and Fgf8 play positive and negative roles for *Mesp2* expression, respectively, we assumed that the increase of *Mesp2* expression occurs when the cNICD activity, n, exceeds that of Fgf8, f, with the amount dependent on n–f. Tbx6 (b) is also required for *Mesp2* expression. We thus modeled the *Mesp2* mRNA expression, m, and Mesp2 protein expression, p, as:

$$m(x,t+\Delta t)=m(x,t)+S_m\times\frac{[\{n(x,t)-f(x,t)\}/K_n]^{H_n}}{1+[\{n(x,t)-f(x,t)\}/K_n]^{H_n}}\times\frac{\{b(x,t)/K_b\}^{H_b}}{1+\{b(x,t)/K_b\}^{H_b}}-D_m\times m(x,t)\,,$$

$$p(x,t+\Delta t)=p(x,t)+S_p\times m(x,t-T)-D_p\times p(x,t)\,,$$

with the initial condition $m(x,0)=0$, and $p(x,0)=0$. The degradation of Tbx6 is dependent on Mesp2 (Oginuma et al., 2008). We introduced a hypothetical molecule, z, that is expressed depending on Mesp2 and degrades Tbx6 by interacting with it. The expression of Tbx6 (b) and the Tbx6 degrading molecule (z) were modeled as:

$$z(x,t+\Delta t)=z(x,t)+S_z\times\frac{\{p(x,t-T)/K_p\}^{H_p}}{1+\{p(x,t-T)/K_p\}^{H_p}}-D_z\times z(x,t)\,,$$

$$b(x,t+\Delta t)=b(x,t)-D_b\times\{b(x,t)\}^{Bb}\times\{z(x,t)\}^{Bz}\,,$$

with the initial condition $z(x,0)=0$, and $b(x,0)=1.0$.

These formulas were implemented using C language. The activities of cNICD (n), Fgf8 (f), Mesp2 (m and p), Tbx6-regulator (z) and Tbx6 (b) were calculated over the ranges $-12.5\leq x\leq -2.5$ and $0\leq t\leq 20$. The calculations were conducted discretely with a single unit of x (Δx) of 1/10 and t (Δt) of 1/10. The parameter values we used are shown in Table S1 in the supplementary material. We also introduced time delay, $T=2\Delta t$, for protein expression (Lewis, 2003), which did not affect the results much.

RESULTS

Dissection of the *Lfng* expression pattern in the PSM

To examine the significance of the Notch on/off state during boundary formation, we focused on *Lfng* expression, which exhibits a biphasic pattern involving oscillation in the posterior PSM and a stabilized striped pattern in the anterior PSM (Aulehla and Johnson, 1999; Cole et al., 2002; McGrew et al., 1998; Morales et al., 2002). Each of these two patterns is implicated in the generation of the corresponding Notch activity profile via negative regulation. To induce only the oscillatory expression of *Lfng*, we utilized the *Hes7* transcriptional regulatory unit as the oscillation of *Lfng* and *Hes7* is regulated by similar factors, i.e. positively by Notch signaling and negatively by Hes7 protein. As shown in Fig. 1, these two transcripts show similar expression patterns in the oscillation phase. Both signals manifest a waved pattern within the Tbx6 expression domain from phase I to phase III (Fig. 1A-L). However, in phases I-II, *Hes7* expression is lost from the anterior domain (Fig. 1G-J), whereas that of *Lfng* persists for a longer period in the anterior PSM and forms a clear stripe (Fig. 1A-D,M,O). It should also be noted that the anterior *Lfng* expression domain was found to merge with that of the Mesp2 protein (Fig. 1N,P), the expression of which is restricted to the anterior PSM. This is not unexpected as *Lfng* expression is induced by Mesp2 in the anterior PSM and creates the Notch on/off state (Morimoto et al., 2005). Taken together, we concluded from these data that the *Lfng* expression pattern can be reproduced by two distinct regulatory systems – the *Hes7* promoter-enhancer and the *Mesp2* regulatory system – and this enabled us to further investigate the significance of Notch activities.

The cNICD on/off state is not required for somite boundary formation

To further elucidate the functional significance of the oscillatory cNICD in the posterior PSM and that of the cNICD on/off state in the anterior PSM, we generated a transgenic mouse line by inserting *Lfng* cDNA flanked with *IRES-EGFP* under the control of the Hes7 promoter (see Fig. S1A in the supplementary material). As expected, the expression pattern of this transgene, examined by in situ hybridization using *EGFP* as a probe, was found to be very similar to that of endogenous *Hes7* and *Lfng* except for the lack of anterior striped expression (see Fig. S1B-D in the supplementary material). We then introduced this transgene into the *Lfng*-null genetic background to establish the *Hes7>Lfng/Lfng*$^{-/-}$ mouse line and examined the expression pattern of exogenous *Lfng* and cNICD expression in the absence of endogenous *Lfng* expression (i.e. an *Lfng*-null background). In wild-type embryos, *Lfng* and cNICD showed biphasic patterns, these being oscillation in the posterior PSM and stabilization in the anterior PSM, whereas cNICD oscillation was barely detectable and a constant level of cNICD could be observed through the entire PSM in the absence of *Lfng*, as reported previously (Morimoto et al., 2005). In the *Hes7>Lfng/Lfng*$^{-/-}$ embryo, however, we observed the recovery of cNICD oscillation in the posterior PSM, which overlapped with *Lfng* expression (Fig. 2A-F), clearly indicating that the *Lfng* transgene was functionally active in these embryos. In addition, we previously showed that cNICD and Mesp2 generate a clear boundary in the anterior PSM, which demarcates the presumptive segmental border in phase-II embryos (Morimoto et al., 2005) (Fig. 2G-I). In the absence of *Lfng*, this clear border between cNICD and Mesp2 was not generated and a merged pattern was instead observed

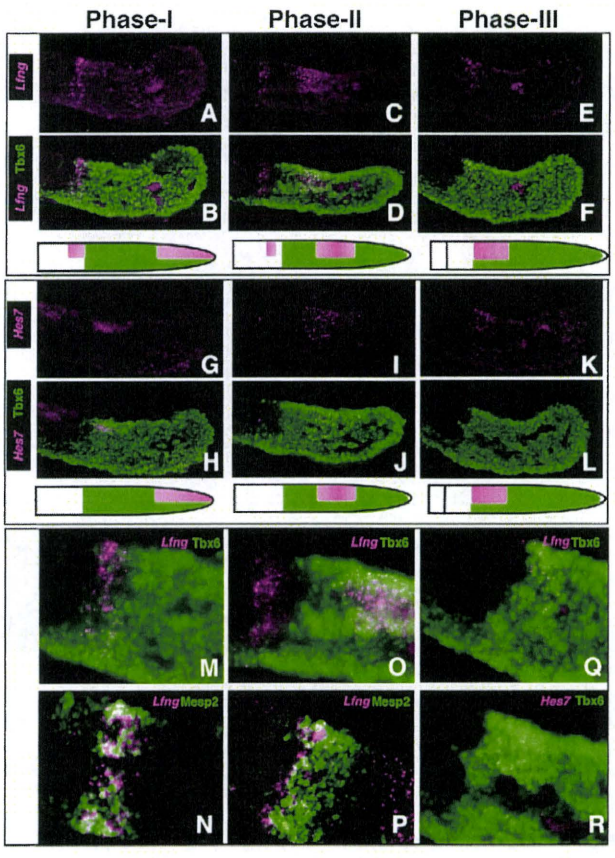

Fig. 1. Comparison of the *Hes7* and *Lfng* expression patterns. In situ hybridization analysis of the spatiotemporal changes in the *Lfng* (**A-F**) and *Hes7* (**G-L**) transcription patterns during somitogenesis by double staining for the Tbx6 protein as the reference point. The stained sections shown in the vertical rows are derived from a single embryo. The phase was defined by the location of the *Hes7* and *Lfng* transcripts and the waves of oscillating *Hes7* and *Lfng* were initiated at the posterior PSM (Phase I). The oscillating wave then moves to the intermediate PSM (Phase II) and reaches the anterior PSM (Phase III). (**M**,**O**,**Q**,**R**) Magnified images of B, D, F and L, respectively. Phase I and Phase II sections were also subjected to double staining for *Lfng* mRNA and Mesp2 (**N**,**P**).

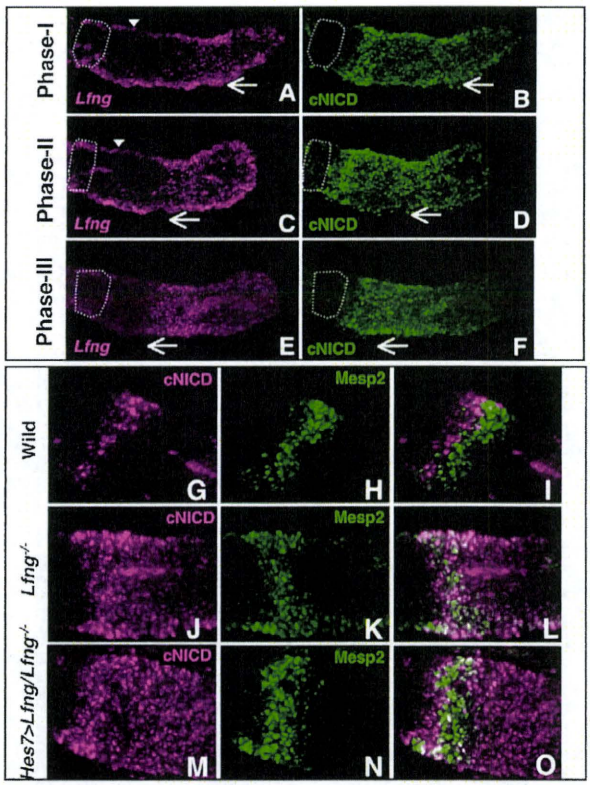

Fig. 2. *Hes7>Lfng/Lfng*$^{-/-}$ mice show cNICD oscillation in the posterior PSM but do not form a cNICD boundary in the anterior PSM. (**A-F**) The patterns of *Lfng* mRNA (A,C,E) and cNICD (B,D,F) expression were revealed in each channel by double staining of these signals using single embryos of *Hes7>Lfng/Lfng*$^{-/-}$ mice at three different phases, I-III, respectively. *Lfng* expression shows a traveling wave (arrow) but no stabilized stripe (arrowheads, A,C). The first somite is indicated by a white dotted line. The wave of oscillating cNICD is initiated at the posterior PSM (B; Phase I; n=3), moves to the intermediate PSM (D; Phase II; n=4) and eventually reaches the anterior PSM (F; Phase III; n=3). (**G-O**) The relationship between cNICD and Mesp2 in Phase II was compared among wild-type (G-I), *Lfng*$^{-/-}$ (J-L) and *Hes7>Lfng/Lfng*$^{-/-}$ (M-O) embryos by double staining. Single channels for cNICD (G,J,M) and Mesp2 (H,K,N), and merged images of both (I,L,O), are shown. In the wild-type embryos, cNICD and Mesp2 generate a clear boundary (I). *Lfng*$^{-/-}$ and *Hes7>Lfng/Lfng*$^{-/-}$ mice, however, do not show a clear segregation between cNICD and Mesp2 (L,O).

(Fig. 2J-L). In the *Hes7>Lfng/Lfng*$^{-/-}$ embryo, as expected by the lack of Lfng expression in the anterior PSM, we did not detect segregation between the cNICD and Mesp2 domains (Fig. 2M-O). *Lfng*$^{-/-}$ embryos did not show clear somite boundaries, although incomplete somites did appear to be formed (see Fig. S2 in the supplementary material), as also suggested previously (Evrard et al., 1998; Zhang and Gridley, 1998). Very surprisingly, however, *Hes7>Lfng/Lfng*$^{-/-}$ embryos showed clearly segmented somites (Fig. 3A-C). This strongly indicates that the oscillatory expression of cNICD mediated via oscillating Lfng is sufficient to provide the conditions for normal somitogenesis to occur and that the cNICD boundary in the anterior PSM is not required for this process.

Recently, we and others have suggested that the Mesp2 downstream events, such as the activation of ephrin-EphA4 signaling and the formation of a Tbx6 protein boundary, were more important for segmental border formation (Watanabe et al., 2009; Oginuma et al., 2008; Nakajima et al., 2006). In *Lfng*$^{-/-}$ embryos, the expression of *EphA4* and the Tbx6 protein boundary were found to be diffuse or randomized (Fig. 3E,J-L), whereas in *Hes7>Lfng/Lfng*$^{-/-}$ embryos, these expression patterns appeared to be normal (Fig. 3F,M-O), i.e. similar to those in wild-type embryos (Fig. 3D,G-I). Taken together, our current findings show that the cNICD boundary is dispensable, but that the Mesp2 boundary might be required, for the creation of the segmental border through the regulation of downstream genes.

R-C polarity is completely recovered in *Hes7>Lfng/Lfng*$^{-/-}$ embryos

We next further examined the morphological features of the *Hes7>Lfng/Lfng*$^{-/-}$ embryo. Surprisingly, these transgenic embryos showed a completely normal skeletal system, with segmented vertebra and ribs (Fig. 4A-C). Furthermore, the expression pattern of *Uncx4.1*, a caudal marker of R-C polarity (Fig. 4D), was fully recovered in the *Hes7>Lfng/Lfng*$^{-/-}$ embryo (Fig. 4F), which contrasts with the randomized pattern we observed in the *Lfng*$^{-/-}$ embryo (Fig. 4E). These results suggest that the cNICD boundary in

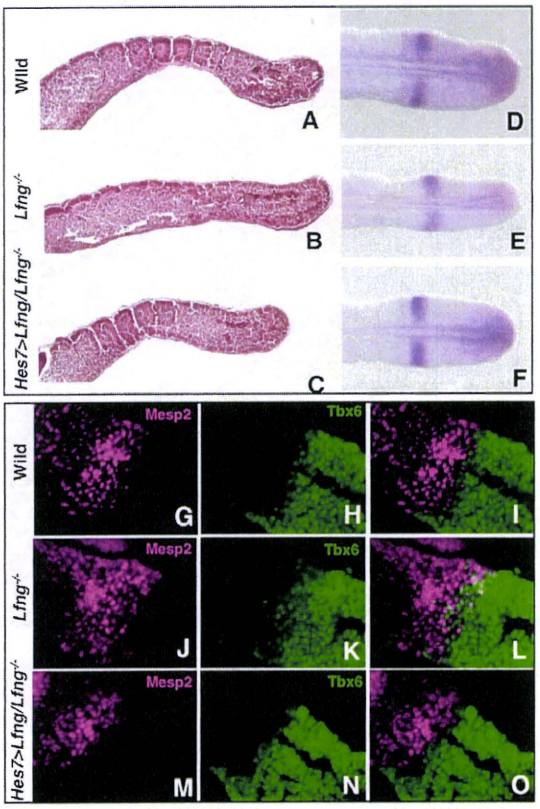

Fig. 3. Exogenous *Lfng* controlled by the *Hes7* promoter completely rescues the boundary formation defect in the *Lfng*$^{-/-}$ mice. The segmental morphologies (**A-C**), the *EphA4* expression pattern (**D-F**) and the relationship between Mesp2 and Tbx6 in Phase II (**G-O**) were compared among wild-type (A,D,G-I), *Lfng*$^{-/-}$ (B,E,J-L) and *Hes7>Lfng/Lfng*$^{-/-}$ (C,F,M-O) using E11.5 embryonic tail regions. Single channels for Mesp2 (G,J,M) and Tbx6 (H,K,N), and merged images of both (I,L,O), are shown. Expression of the *EphA4* and Tbx6 protein boundary forms a clear border in the wild-type (D, *n*=7; G-I, *n*=4) and *Hes7>Lfng/Lfng*$^{-/-}$ embryos (F, *n*=4; M-O, *n*=4), but this is diffuse or randomized in the *Lfng*$^{-/-}$ embryos (E, *n*=4; J-L, *n*=3).

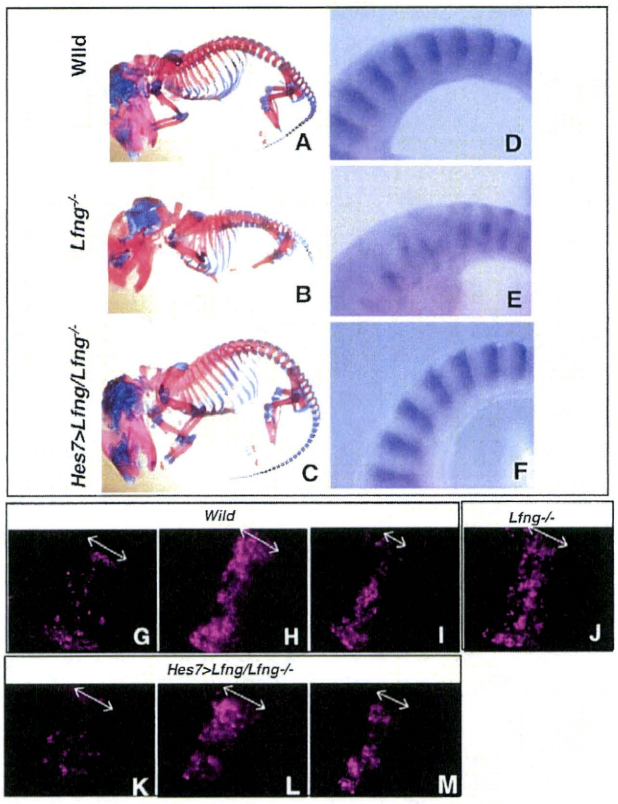

Fig. 4. Exogenous *Lfng* under the control of the *Hes7* promoter completely rescues the R-C patterning defect in the somites of *Lfng*$^{-/-}$ mice. A comparison of the segmental morphologies of skeletal preparations of E17.5 embryos (**A-C**) and the expression pattern of *Uncx4.1*, indicative of R-C patterning within a somite (**D-F**). *Hes7>Lfng/Lfng*$^{-/-}$ mice show a normal skeleton (C, *n*=4) and expression pattern of *Uncx4.1* (F, *n*=3), whereas *Lfng*$^{-/-}$ mice show randomized pattern of skeleton (B) and *Uncx4.1* expression (E). (**G-M**) *Mesp2* transcription states revealed by high resolution in situ hybridization analysis of wild-type embryos for transcriptional initiation (G, *n*=3), active state (H, *n*=5) and rostral localization (I, *n*=3), and *Lfng*-null (J, *n*=11) and *Hes7>Lfng/Lfng*$^{-/-}$ embryos for transcriptional initiation (K, *n*=2), active state (L, *n*=3) and rostral localization (M, *n*=3). Double arrows indicate the length of the *Mesp2* transcription domains.

the anterior PSM is not required for normal R-C polarity patterning. To elucidate this issue further, we focused on the expression of *Mesp2*, which is thought to be the final output signal of the segmentation clock. *Mesp2* is initially expressed over one somite length and then becomes localized in the rostral compartment (Takahashi et al., 2000). This dynamic expression pattern generates a gradient of Mesp2 activity that allows PSM cells to form the R-C pattern within a somite (Takahashi et al., 2003; Takahashi et al., 2000). We therefore next compared the *Mesp2* expression pattern at the cellular level among the wild-type, *Lfng*$^{-/-}$ and *Hes7>Lfng/Lfng*$^{-/-}$ embryos using high-resolution in situ hybridization. By focusing on the length of the *Mesp2* transcription domain along the A-P axis, we found four distinct patterns in the wild-type embryos: (1) no signal (n=4/15); (2) most cells show nuclear dots indicating transcriptional initiation, and the length of the *Mesp2* transcription domain is approximately 11-13 cells (Fig. 4G; n=3/15); (3) active stage in which signals can be observed in the cytoplasm in addition to nuclear dots, and the length of *Mesp2* transcription is approximately 10-12 cells, with anterior cells showing stronger signals (Fig. 4H; n=5/15); and (4) rostral localization in which the length of the *Mesp2* transcription domain becomes approximately 5-6 cells (Fig. 4I; n=3/15). In contrast to wild-type embryos, only one pattern was observed in the *Lfng*-null embryos: signals were observed in the cytoplasm in addition to nuclear dots, the expression levels were randomized for each cells, and the length of the *Mesp2* transcription domain was approximately 9-11 cells (Fig. 4J; n=11/11). These results indicate that *Mesp2* expression is always present in the anterior PSM without clear on/off cycles in the *Lfng*-null embryo. In addition, the *Mesp2* expression domain is kept to one somite length and there is no clear localization into the rostral compartment, although cellular or cell cluster-level localization might occur in a salt-and-pepper pattern in the absence of Lfng. Importantly, the *Mesp2* expression pattern was found to show four distinct patterns similar to those in wild-type embryos even in the *Hes7>Lfng/Lfng*$^{-/-}$ embryos, i.e. no signal (1/9), transcriptional initiation (Fig. 4K, n=2/9), active stage (Fig. 4L, n=3/9) and rostral localization (Fig. 4M; n=3/9). Our findings thus indicate that the oscillation of cNICD alone is sufficient to generate the normal *Mesp2* expression pattern and that the anterior PSM-specific regulation of cNICD via Lfng is dispensable for this process.

Modeling of the *Mesp2* expression pattern

To test the validity of our above hypothesis, we performed computer simulations. Our model is based on that previously proposed by Lewis and colleagues, in which the oscillatory waves emanate, travel and eventually cease, as it adopts the notion of maturity, which delays the oscillation cycle towards the anterior as time proceeds (Palmeirim et al., 1997). In this model of Lewis, the cessation of the oscillatory waves triggers periodic gene expression along an anterior-posterior direction that leads to the formation of the somites (Palmeirim et al., 1997). In our current study, we applied the Lewis model to the oscillatory waves of the cNICD and assumed Fgf as a molecular basis for maturity. We further incorporated the regulatory network required for *Mesp2* expression, in which cNICD oscillation and Tbx6 synergistically activate (Yasuhiko et al., 2006; Oginuma et al., 2008), whereas the Fgf gradient suppresses *Mesp2* expression and Tbx6 is degraded downstream of Mesp2 (Fig. 5A). Very surprisingly, this simple simulation successfully mimicked some specific features of dynamic *Mesp2* transcription (red line), not only in terms of on/off cycles but also with regard to temporal changes in the expression pattern (from one somite length to rostral localization) along the anterior-posterior axis (Fig. 5B; see Movie 1 in the supplementary material), similar to that observed in vivo (Fig. 4G-I; see Fig. S3A,B in the supplementary material). In addition, this simulation also reproduced the gradient of Mesp2 activity accumulation (black line), which is similar to the *Mesp2*-β-gal pattern we observed in the *Mesp2*$^{lacZ/+}$ embryos (see Fig. S3E in the supplementary material).

To test the importance of the cNICD wave for the gradient formation of Mesp2 activity, we examined *Mesp2* expression under constant activity of cNICD in the PSM (Fig. 5C; see Movie 2 in the supplementary material). In this instance, *Mesp2* expression is always observed in the anterior PSM without either clear on/off cycles or localization at the rostral compartment, which is very similar to the in vivo situation of the *Lfng*$^{-/-}$ embryos (Fig. 4J; see Fig. S3C,D,F in the supplementary material). Interestingly, in our model, neither the formation of the waved pattern of cNICD nor its migration is necessary to establish the gradient of Mesp2 activity because a spatially uniform, but temporally oscillating, Notch signaling activity is sufficient to reproduce this gradient (see Fig. S4 and Movie 3 in the supplementary material). Without a traveling wave, however, the temporal transition of the Mesp2 expression pattern from a one-somite length to a rostral localization was not reproduced (see Fig. S4 and Movie 3 in the supplementary material). We thus speculate that this transition might be important for robust somite formation with a correct R-C polarity and propose that the wave of Notch activity enables PSM cells to establish not only the periodic expression of *Mesp2*, but also their localization into the rostral compartment. Our model therefore provides a new concept that indicates that a progressive oscillating wave of Notch activity is translated into the R-C polarity of a somite through the regulation of the Mesp2 expression pattern.

Anterior PSM-specific *Lfng* cannot rescue the defects in *Mesp2*-null or *Lfng*-null mice

Finally, to further ask the significance of the anterior striped cNICD domain for somite boundary formation, we established a mouse line that reproduces this expression pattern by introducing *Lfng* cDNA at the *Mesp2* locus using embryonic stem cell-mediated homologous recombination (see Fig. S1E in the supplementary material). The resulting heterozygous mice showed no abnormalities and we generated an intercross of *Mesp2*$^{Lfng/+}$ to yield *Mesp2*$^{Lfng/Lfng}$. In the *Mesp2*$^{Lfng/Lfng}$ embryos, cNICD signals were suppressed in the *Lfng*-expressing cells in the anterior PSM (Fig. 6B), as seen in the wild type (Fig. 6A). We further found that some of the cells that did not express *Lfng* maintained cNICD signals, indicating that Lfng suppresses cNICD production in a cell-autonomous manner (Fig. 6D). However, Lfng did not rescue the phenotype of the *Mesp2*-null mice (Fig. 6H-M), indicating that the function of *Lfng* downstream of *Mesp2* is not important.

We next introduced this transgene into the *Lfng*-null genetic background to generate a *Mesp2*$^{Lfng/+}$*Lfng*$^{-/-}$ mouse. The expression levels of *Lfng* in the *Mesp2* locus were found to be low (Fig. 6C,E; see Fig. S5C in the supplementary material), but we did observe downregulation of the cNICD signal in the *Mesp2*-expressing cells (Fig. 6F) in comparison with the *Lfng*-null embryos (Fig. 6G). Furthermore, *Hes5* expression (see Fig. S5D in the supplementary material), a target gene of Notch signaling, was severely downregulated in both the *Mesp2*$^{Lfng/Lfng}$ and *Mesp2*$^{Lfng/+}$*Lfng*$^{-/-}$ embryos (see Fig. S5F,H in the supplementary material) compared with *Mesp2*- and *Lfng*-null embryos (see Fig. S5E,G in the supplementary material), indicating that *Lfng* under the control of *Mesp2* might effectively suppress Notch signaling. However, we did

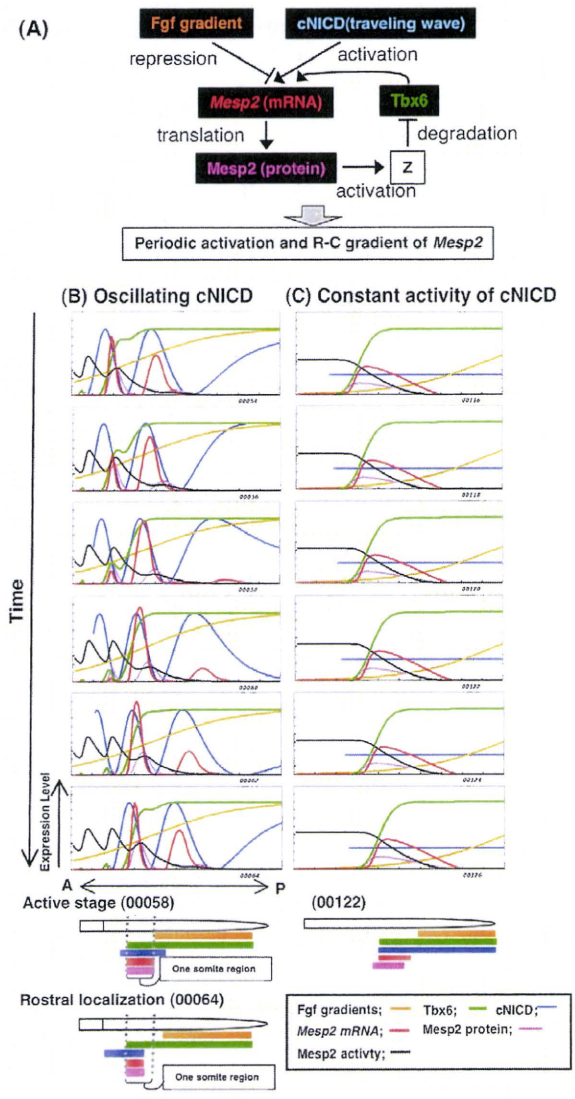

Fig. 5. Model of *Mesp2* expression. (**A**) Schematic representation indicating relationships among *Mesp2* mRNA, Mesp2 protein, Tbx6, cNICD and Fgf signaling, which is used for computer simulation to reproduce the periodic activation and R-C gradient of *Mesp2* expression. z is a hypothetical molecule that functions downstream of Mesp2 and mediates negative-feedback regulation of Tbx6. (**B**,**C**) Expression patterns of *Mesp2*, cNICD and other proteins along the anteroposterior axis predicted in our numerical model. Snapshot images of computer simulations of one cycle of somite formation in the presence (B) or absence (C) of cNICD oscillation are shown. Colored lines indicate levels of cNICD (blue), Fgf8 (orange), *Mesp2* expression (mRNA, red line; protein, pink line) and Tbx6 (green). Mesp2 activity, reflecting the total accumulation of Mesp2 protein, is shown as a tracking line in black. Data sets were taken from Movies 1 (frame 54-64) and 2 (frame 116-126) in the supplementary material, respectively. cNICD (blue) was made to disappear in the panels after one somite is formed, according to experimental observations (Morimoto et al., 2005; Oginuma et al., 2008). Lower diagrams indicate the relationships among these factors at critical time points. Snapshot (00058) corresponds to the transcriptionally active stage of *Mesp2* in which a cNICD wave (blue) reaches the anterior PSM and *Mesp2* (red) is activated in the one-somite region. Snapshot (00064) corresponds to the rostral localization stage, i.e. following the anterior shift of the cNICD wave, the *Mesp2* expression domain also shifts to the rostral region, generating a gradient of Mesp2 activity (black). As the level of cNICD is constant in the *Lfng*-null situation [corresponding to snapshot (00112)], *Mesp2* expression (red) does not show a dynamic pattern and regresses posteriorly.

not detect any significant rescue of the segmental morphology in the developing embryos or of the vertebral morphology at any level along the anteroposterior axis in the $Mesp2^{Lfng/+}Lfng^{-/-}$ mice compared with the *Lfng*-null mouse (Fig. 6N-Q; see Fig. S6 in the supplementary material). These results further confirmed that the suppression of cNICD signaling by stabilized Lfng is not sufficient for normal somitogenesis to occur.

DISCUSSION

The requirement for Notch signaling during mouse somitogenesis

In our current study, we reveal that the cNICD on/off state is not required for somite boundary formation during somitogenesis in the mouse. Consistent with this, recent studies in zebrafish embryos suggest that the function of Notch signaling is only to synchronize the oscillations among PSM cells, and that this pathway has no other function during segmentation (Riedel-Kruse et al., 2007; Horikawa et al., 2006; Ozbudak and Lewis, 2008). However, we propose from our current data that Notch signaling has a crucial function also as an output of the segmentation clock during mouse development. This contention is supported by earlier evidence that *Mesp2* expression is severely downregulated in the absence of Notch signaling (Barrantes et al., 1999; Takahashi et al., 2000). Moreover, it has been shown that constitutive activation of Notch signaling in the paraxial mesoderm induces *Mesp2* transcription without clear on/off cycles (Feller et al., 2008) and it is also evident from other reports that Notch signaling is crucial for the establishment of R-C patterning of somites in the mouse (Takahashi et al., 2000; Takahashi et al., 2003; Feller et al., 2008). These results together suggest that the function of Notch signaling is not only to synchronize oscillations but that Notch acts also as an important output signal of the segmentation clock, at least in mouse somitogenesis. We thus speculate that Notch signaling is a key factor that mediates the transduction of clock activities into the morphological segmental pattern by regulating *Mesp2* expression. However, it is known that several oscillating components in Notch, Wnt and Fgf signaling pathways are coordinated to generate the segmentation clock network in mice. Hence, *Mesp2* transcription might not be regulated by Notch signaling alone and several pathways might govern the spatiotemporal pattern of *Mesp2* expression. The coordination of these complex networks might well be fundamental to normal somitogenesis.

A new model for the establishment of R-C polarity during somitogenesis

Based on our present findings, we propose a new function for oscillating Notch signaling, which is translated into the R-C polarity of a somite via the regulation of *Mesp2* expression in the anterior PSM. Previous models have proposed that the establishment of R-C polarity requires cell-cell communication (Takahashi et al., 2003; Dale and Pourquie, 2000), whereas we propose a model in which a

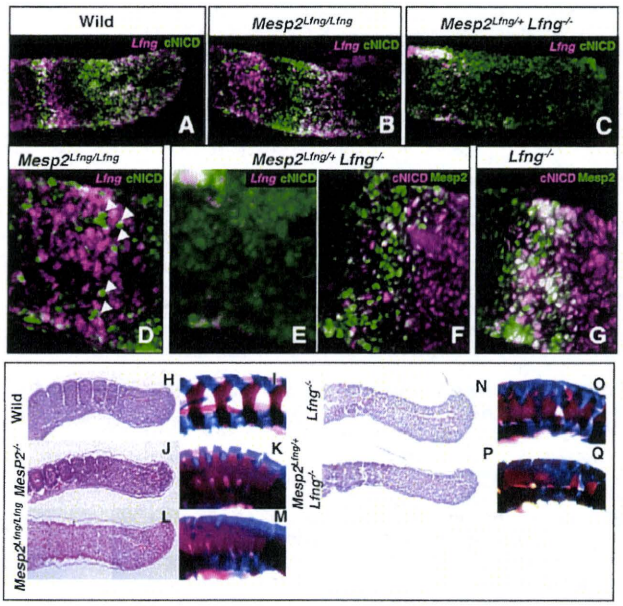

Fig. 6. Exogenous *Lfng* under the control of the *Mesp2* promoter does not rescue the phenotype of the *Mesp2*$^{-/-}$ or *Lfng*$^{-/-}$ mouse. (**A-G**) Sections of E11.5 embryos double stained for *Lfng* mRNA and cNICD (A-E) or for Mesp2 and cNICD (F,G). Higher magnification images of B and C are shown in D and E, respectively. In the *Mesp2*$^{Lfng/Lfng}$ embryo, cNICD formation (B,D, *n*=3) is suppressed in the anterior PSM. The arrowheads in D indicate *Lfng* non-expressing cells that maintain cNICD formation cell-autonomously. In the *Mesp2*$^{Lfng/+}$*Lfng*$^{-/-}$ embryos, cNICD (F, *n*=5) is effectively suppressed in the Mesp2-expressing cells compared with *Lfng*-null embryos (G, *n*=6). (**H-Q**) Comparison of the segmental morphologies in the E11.5 embryonic tail region (H,J,L,N,P) and E17.5 vertebral region (I,K,M,O,Q) among the different genotypes indicated. Neither the *Mesp2*$^{Lfng/Lfng}$ (L,M) nor *Mesp2*$^{Lfng/+}$*Lfng*$^{-/-}$ (P,Q) mice show any recovery of the *Mesp2*$^{-/-}$ (J,K) or *Lfng*$^{-/-}$ (N,O) phenotypes. Number of samples: H, *n*=4; I, *n*=6; J, *n*=3; K, *n*=4; L, *n*=3; M, *n*=6; N, *n*=3; O, *n*=6; P, *n*=3; Q, *n*=7.

cell-autonomous mechanism utilizes Notch signaling oscillation in the posterior PSM. This notion is further supported by computer simulations, in which we found that an appropriate translation of spatiotemporal information provided by the traveling wave of cNICD is sufficient to create the dynamic *Mesp2* expression pattern, i.e. on/off cycles and rostral localization (Fig. 5B; see Movie 1 in the supplementary material). In these simulation experiments, the generation of the traveling wave was based on the earlier work of Lewis (Palmeirim et al., 1997), and the translation of the wave information into *Mesp2* expression was modeled on the gene network that we elucidated previously (Oginuma et al., 2008; Yasuhiko et al., 2006). In the model, the cNICD wave, an activator of *Mesp2*, travels from the posterior to the anterior, whereas the levels of Fgf, a repressor of *Mesp2*, are higher toward the posterior. Consequently, as a single wave passes through a nascent somite, the net transcriptional activation of *Mesp2*, which reflects the amount of cNICD subtracted by the amount of Fgf, is higher toward the rostral part of the presumptive somite. The resulting gradient of Mesp2 activity might thus allow PSM cells to establish a rostral identity and the segmental border. Hence, this is the first model to demonstrate that R-C polarity in the somite is generated as a direct output of the segmentation clock.

The repression of Tbx6, an activator of *Mesp2*, downstream of Mesp2 is another important component in our model. This regulatory module prevents *Mesp2* expression after one traveling wave of cNICD has passed, and thus fixes the R-C gradient pattern of Mesp2. The next wave of Notch signaling cannot affect the Mesp2 pattern created by the former wave. To reproduce the intensive degradation of Tbx6 at anterior regions, we had to adjust the parameters for Tbx6 degradation. We did not need to change any of the other standard parameters we initially chose, suggesting that the qualitative features of the model are not so sensitive to the quantitative values of the parameters. In our simulation analysis, however, we did not reproduce the sharp anterior boundaries of Tbx6 and Mesp2 accumulation (green and black lines, respectively, in Fig. 5B; see Movie 1 in the supplementary material) that have been observed in vivo. To create a sharp boundary of Tbx6 and Mesp2, which should be required to create a fine segmentation boundary, further adjustment of the parameters or another mechanism might be required. In this regard, the next important challenge will be to investigate the molecular basis of the sharpening expression boundaries of Tbx6 and Mesp2, and ultimately to understand how analog inputs (such as sequential wave patterns of oscillation) are converted into digital outputs (such as the square-like stair patterns of the segmental border).

Functions of Lfng in the posterior and anterior PSM during mouse somitogenesis

We also demonstrate from our present data that the oscillatory expression of *Lfng* is both required and sufficient for normal somitogenesis. However, this result will probably be viewed somewhat controversially given the recent findings that have underscored the significance of Lfng expression in the anterior PSM during this process, at least after E10.5 (Shifley et al., 2008; Stauber et al., 2009). The authors of these reports produced transgenic mice harboring *Lfng* expression without oscillation. Their data indicate that cNICD oscillation is disrupted, but that normal segmented somites form, after E10.5 and they concluded that oscillating *Lfng* expression is required only for early stage, but not later stage, somitogenesis (Shifley et al., 2008; Stauber et al., 2009). We wish therefore to discuss some possible explanations for the discrepancies between our current findings and these previous experimental results.

One possibility is that the common expression profiles between our *Hes7>Lfng* mouse and the mice studied in previous reports is important. We demonstrate here that *Hes7* and *Lfng* expression manifest a waved pattern within the Tbx6 expression domain, which includes a part of the anterior PSM. Therefore, in our *Hes7>Lfng* mouse, oscillating *Lfng* expression also exists in the anterior PSM, but not as a stabilized pattern. We suspect that the transgenic mice analyzed in previous reports lack oscillating *Lfng* expression in the posterior PSM but the oscillation might exist in the anterior PSM as well, and thus we speculate that the oscillating *Lfng* expression in the posterior PSM is not required after E10.5, but that in the anterior PSM might be sufficient for normal somitogenesis. Another possibility is that the slightly oscillating expression reported previously might be responsible for the rescue event. Previous studies have shown that two distinct enhancers are involved in the oscillatory expression of *Lfng*, one of which is disrupted in the mouse reported by Shifley et al. (Shifley et al., 2008), and a slight cyclic expression of *Lfng* exists in the mouse generated by Stauber et al. (Stauber et al., 2009). Hence, one possible interpretation for these discrepancies is that the slight cyclic expression of *Lfng* might be sufficient for normal development in the enhancer-specific

knockout mouse after E10.5 somitogenesis, but not prior to E10.5. It is reasonable to assume that the requirement of Notch clock oscillation by *Lfng* changes during somitogenesis and is lesser at later stages, as now suggested by a number of studies (Shifley et al., 2008; Stauber et al., 2009).

Acknowledgements
We thank Ryoichiro Kageyama (Kyoto University) for providing the *Hes7* promoter and enhancer cassette, Aya Satoh, Nobuo Sasaki and Yusuke Okubo (National Institute of Genetics) for animal care and the preparation of embryo samples and Mariko Ikumi, Eriko Ikeno and Shinobu Watanabe (National Institute of Health Sciences) for technical assistance. This work was supported in part by Grants-in-Aid for Scientific Research on Priority Areas, Dynamics of Extracellular Environments, and by the National BioResource Project from the Ministry of Education, Culture, Sports, Science and Technology, Japan.

Competing interests statement
The authors declare no competing financial interests.

Supplementary material
Supplementary material for this article is available at
http://dev.biologists.org/lookup/suppl/doi:10.1242/dev.044545/-/DC1

References

Aulehla, A. and Johnson, R. L. (1999). Dynamic expression of lunatic fringe suggests a link between notch signaling and an autonomous cellular oscillator driving somite segmentation. *Dev. Biol.* **207**, 49-61.
Aulehla, A., Wehrle, C., Brand-Saberi, B., Kemler, R., Gossler, A., Kanzler, B. and Herrmann, B. G. (2003). Wnt3a plays a major role in the segmentation clock controlling somitogenesis. *Dev. Cell* **4**, 395-406.
Aulehla, A., Wiegraebe, W., Baubet, V., Wahl, M. B., Deng, C., Taketo, M., Lewandoski, M. and Pourquie, O. (2008). A beta-catenin gradient links the clock and wavefront systems in mouse embryo segmentation. *Nat. Cell Biol.* **10**, 186-193.
Barrantes, I. B., Elia, A. J., Wunsch, K., Hrabe de Angelis, M. H., Mak, T. W., Rossant, J., Conlon, R. A., Gossler, A. and de la Pompa, J. L. (1999). Interaction between Notch signalling and Lunatic fringe during somite boundary formation in the mouse. *Curr. Biol.* **9**, 470-480.
Bessho, Y., Hirata, H., Masamizu, Y. and Kageyama, R. (2003). Periodic repression by the bHLH factor Hes7 is an essential mechanism for the somite segmentation clock. *Genes Dev.* **17**, 1451-1456.
Cole, S. E., Levorse, J. M., Tilghman, S. M. and Vogt, T. F. (2002). Clock regulatory elements control cyclic expression of Lunatic fringe during somitogenesis. *Dev. Cell* **3**, 75-84.
Dale, K. J. and Pourquie, O. (2000). A clock-work somite. *BioEssays* **22**, 72-83.
Delfini, M. C., Dubrulle, J., Malapert, P., Chal, J. and Pourquie, O. (2005). Control of the segmentation process by graded MAPK/ERK activation in the chick embryo. *Proc. Natl. Acad. Sci. USA* **102**, 11343-11348.
Dequeant, M. L. and Pourquie, O. (2008). Segmental patterning of the vertebrate embryonic axis. *Nat. Rev. Genet.* **9**, 370-382.
Dequeant, M. L., Glynn, E., Gaudenz, K., Wahl, M., Chen, J., Mushegian, A. and Pourquie, O. (2006). A complex oscillating network of signaling genes underlies the mouse segmentation clock. *Science* **314**, 1595-1598.
Evrard, Y. A., Lun, Y., Aulehla, A., Gan, L. and Johnson, R. L. (1998). lunatic fringe is an essential mediator of somite segmentation and patterning. *Nature* **394**, 377-381.
Feller, J., Schneider, A., Schuster-Gossler, K. and Gossler, A. (2008). Noncyclic Notch activity in the presomitic mesoderm demonstrates uncoupling of somite compartmentalization and boundary formation. *Genes Dev.* **22**, 2166-2171.
Horikawa, K., Ishimatsu, K., Yoshimoto, E., Kondo, S. and Takeda, H. (2006). Noise-resistant and synchronized oscillation of the segmentation clock. *Nature* **441**, 719-723.
Lewis, J. (2003). Autoinhibition with transcriptional delay: a simple mechanism for the zebrafish somitogenesis oscillator. *Curr. Biol.* **13**, 1398-1408.
McGrew, M. J., Dale, J. K., Fraboulet, S. and Pourquie, O. (1998). The lunatic fringe gene is a target of the molecular clock linked to somite segmentation in avian embryos. *Curr. Biol.* **8**, 979-982.
Morales, A. V., Yasuda, Y. and Ish-Horowicz, D. (2002). Periodic Lunatic fringe expression is controlled during segmentation by a cyclic transcriptional enhancer responsive to notch signaling. *Dev. Cell* **3**, 63-74.
Morimoto, M., Takahashi, Y., Endo, M. and Saga, Y. (2005). The Mesp2 transcription factor establishes segmental borders by suppressing Notch activity. *Nature* **435**, 354-359.
Nakajima, Y., Morimoto, M., Takahashi, Y., Koseki, H. and Saga, Y. (2006). Identification of Epha4 enhancer required for segmental expression and the regulation by Mesp2. *Development* **133**, 2517-2525.
Niwa, Y., Masamizu, Y., Liu, T., Nakayama, R., Deng, C. X. and Kageyama, R. (2007). The initiation and propagation of Hes7 oscillation are cooperatively regulated by Fgf and notch signaling in the somite segmentation clock. *Dev. Cell* **13**, 298-304.
Oginuma, M., Niwa, Y., Chapman, D. L. and Saga, Y. (2008). Mesp2 and Tbx6 cooperatively create periodic patterns coupled with the clock machinery during mouse somitogenesis. *Development* **135**, 2555-2562.
Ozbudak, E. M. and Lewis, J. (2008). Notch signalling synchronizes the zebrafish segmentation clock but is not needed to create somite boundaries. *PLoS Genet.* **4**, e15.
Palmeirim, I., Henrique, D., Ish-Horowicz, D. and Pourquie, O. (1997). Avian hairy gene expression identifies a molecular clock linked to vertebrate segmentation and somitogenesis. *Cell* **91**, 639-648.
Riedel-Kruse, I. H., Muller, C. and Oates, A. C. (2007). Synchrony dynamics during initiation, failure, and rescue of the segmentation clock. *Science* **317**, 1911-1915.
Sakai, K. and Miyazaki, J. (1997). A transgenic mouse line that retains Cre recombinase activity in mature oocytes irrespective of the cre transgene transmission. *Biochem. Biophys. Res. Commun.* **237**, 318-324.
Shifley, E. T., Vanhorn, K. M., Perez-Balaguer, A., Franklin, J. D., Weinstein, M. and Cole, S. E. (2008). Oscillatory lunatic fringe activity is crucial for segmentation of the anterior but not posterior skeleton. *Development* **135**, 899-908.
Stauber, M., Sachidanandan, C., Morgenstern, C. and Ish-Horowicz, D. (2009). Differential axial requirements for lunatic fringe and Hes7 transcription during mouse somitogenesis. *PLoS One* **4**, e7996.
Takahashi, Y., Koizumi, K., Takagi, A., Kitajima, S., Inoue, T., Koseki, H. and Saga, Y. (2000). Mesp2 initiates somite segmentation through the Notch signalling pathway. *Nat. Genet.* **25**, 390-396.
Takahashi, Y., Inoue, T., Gossler, A. and Saga, Y. (2003). Feedback loops comprising Dll1, Dll3 and Mesp2, and differential involvement of Psen1 are essential for rostrocaudal patterning of somites. *Development* **130**, 4259-4268.
Takahashi, Y., Yasuhiko, Y., Kitajima, S., Kanno, J. and Saga, Y. (2007). Appropriate suppression of Notch signaling by Mesp factors is essential for stripe pattern formation leading to segment boundary formation. *Dev. Biol.* **304**, 593-603.
Wahl, M. B., Deng, C., Lewandoski, M. and Pourquie, O. (2007). FGF signaling acts upstream of the NOTCH and WNT signaling pathways to control segmentation clock oscillations in mouse somitogenesis. *Development* **134**, 4033-4041.
Watanabe, T., Sato, Y., Saito, D., Tadokoro, R. and Takahashi, Y. (2009). EphrinB2 coordinates the formation of a morphological boundary and cell epithelialization during somite segmentation. *Proc. Natl. Acad. Sci. USA* **106**, 7467-7472.
Yasuhiko, Y., Haraguchi, S., Kitajima, S., Takahashi, Y., Kanno, J. and Saga, Y. (2006). Tbx6-mediated Notch signaling controls somite-specific Mesp2 expression. *Proc. Natl. Acad. Sci. USA* **103**, 3651-3656.
Zhang, N. and Gridley, T. (1998). Defects in somite formation in lunatic fringe-deficient mice. *Nature* **394**, 374-377.